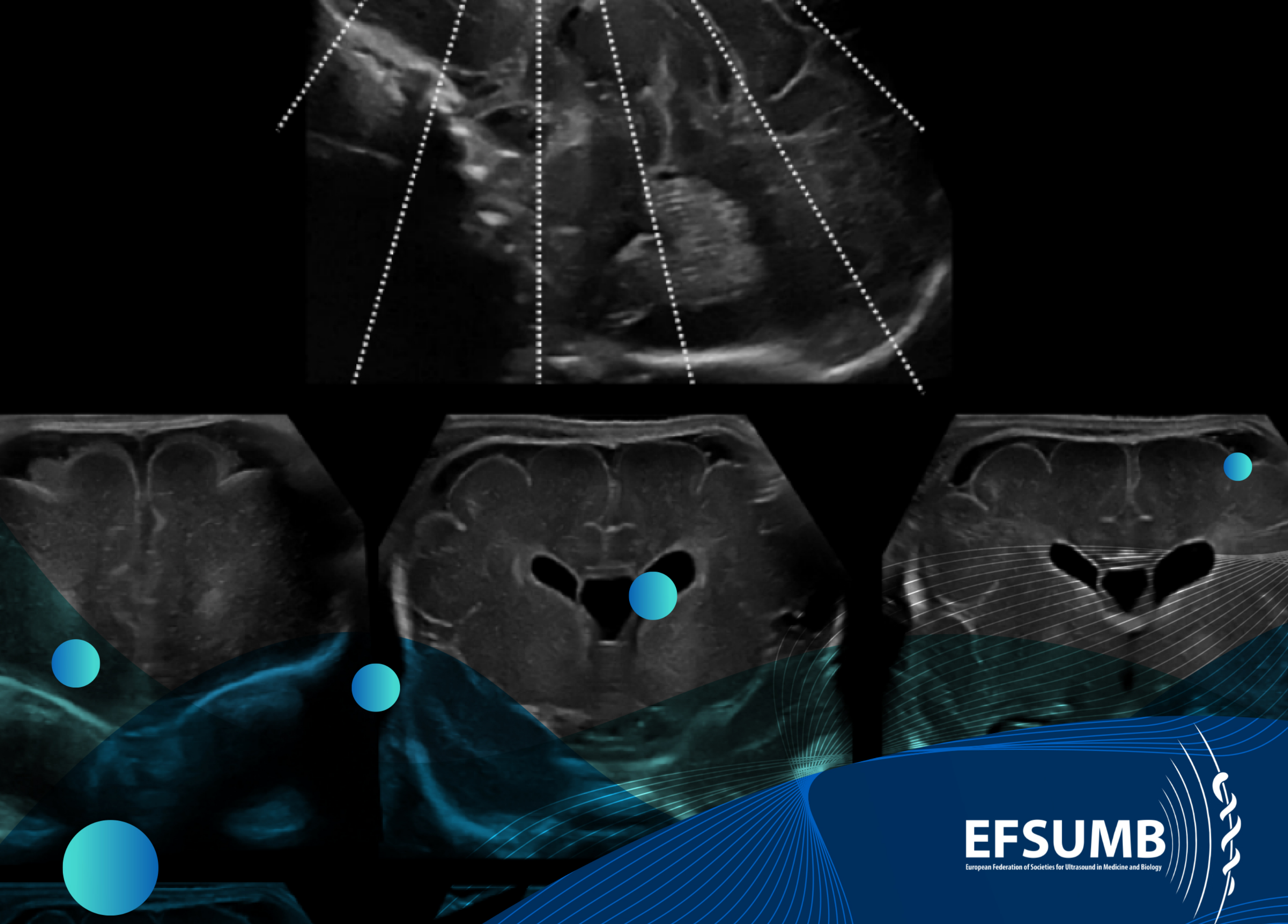

EFSUMB Course Book

Editor: Christoph F. Dietrich

2nd Edition

Ch 45: Neonatal cranial ultrasound: technique, normal anatomy, and common pathologies

Simone Schwarz[1], Tobias Mühlbacher[3], Sandra Horsch[4]

1. University Duisburg-Essen, University Hospital Essen, Department for Pediatrics I, Essen, Germany;
2. Department of Neonatology and Pediatric Intensive Care Medicine, Sana Hospital Duisburg, Duisburg, Germany;
3. University Hospital Zurich, Department of Neonatology, Zurich, Switzerland;
4. Department of Neonatology, Helios Klinikum Berlin Buch, Berlin, Germany

Corresponding author: Dr. med. Simone Schwarz
University Duisburg-Essen, University Hospital Essen, Department for Pediatrics I, Essen, Germany

E-Mail: simone.schwarz@uk-essen.de

Neonatal cranial ultrasound: technique, normal anatomy, and common pathologies

Introduction

Cranial ultrasound (CUS) is a safe, rapid, and radiation-free bedside imaging technique for assessing the brain of newborns and young infants. It reliably detects the most common congenital and acquired brain abnormalities and identifies patients requiring further investigation with other imaging modalities such as magnetic resonance imaging (MRI), angiography, or — in rare cases — computed tomography (CT). Open fontanelles, thin cranial bones, and preexisting foramina can serve as acoustic windows. CUS is widely available and can be used even in the most critically ill patients on neonatal and pediatric intensive care units (NICU/PICU). Although CUS imaging is generally considered safe even in the most immature infants, it can cause discomfort and minor thermal as well as mechanical effects, therefore CUS should always be performed according to the ALARA (as-low-as-reasonably-achievable) principle.

Device Settings and Image Optimization

To image the neonatal brain, both phased array (multi-frequency convex) and linear transducers can be used. For high-quality imaging in neonates, frequencies above 7.5 MHz are recommended (1). Linear probes with frequencies above 10 MHz can produce impressive high-resolution images of superficial structures and are also capable to penetrate the whole brain of small preterm infants (Figure 1). This makes them particularly attractive for use in the most immature patient group. However, in young infants, lower frequencies may sometimes be necessary to achieve better penetration and clearer visualization of deeper brain structures.

Modern ultrasound devices include neonatal CUS presets that allow immediate high-quality scanning. Nevertheless, optimal image quality requires individual adjustment of settings throughout the examination. Investigators should therefore be familiar with adjustments of the frequency (Figure 2), depth (Figure 3), image width/zoom, time gain compensation (TGC), gain, dynamic range (DR) (Figure 4) and focus points.

Figure 1 High-resolution cranial ultrasound. High-resolution CUS in a preterm infant of 24 postmenstrual weeks. Images with a high-frequency linear transducer from the anterior fontanelle (left image) and the temporal bone (middle and right image). 1 = internal capsule, 2 = anterior commissure, 3 = temporal lobe, 4 = hippocampal formation, 5 = midbrain.

Figure 2 Effect of frequency on image quality. High-frequency settings (left) provide superior resolution but limited penetration depth, optimizing visualization of superficial brain structures at the cost of reduced posterior fossa detail when imaging through the anterior fontanelle. Low-frequency settings (right) improve penetration of deeper brain regions, including the posterior fossa, but at the expense of spatial resolution.

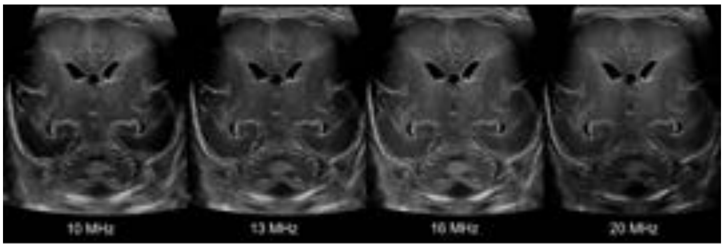

Figure 3 Effect of depth settings on image quality. Three coronal planes at increasing depth settings (left to right). At decreased depth (left image), deeper structures such as the posterior fossa are not visualized. At optimal depth (middle image), all relevant anatomy from the cortex to the posterior fossa is included with appropriate resolution. Increased depth (right image) reduces the apparent size of brain structures and diminishes image resolution.

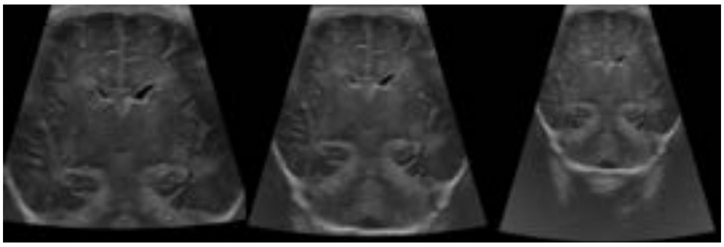

Figure 4 **Effect of the Dynamic Range (DR) settings on image quality. Five coronal planes of the same neonatal brain obtained at increasing DR settings (DR 36, 42, 66, 78, and 96, left to right). At low DR settings (DR 36–42), high contrast makes structures stand out sharply but suppresses subtle grey-scale differences, obscuring soft tissue detail. At intermediate settings (DR 66), a balanced contrast allows adequate differentiation of grey and white matter. At high DR settings (DR 78–96), the increased number of grey shades improves visualization of fine structural detail.**

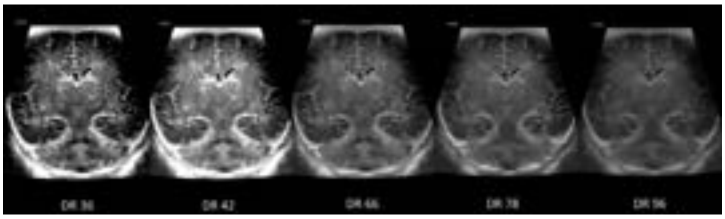

Indications and Timeline

Although there is no international consensus on the indication and timing of routine imaging in preterm and term neonates, it is generally agreed that all admitted neonates and young infants who present with neurological symptoms should be scanned as soon as possible after admission to rule out conditions that might need immediate intervention and to guide further diagnostics and therapy (1). An admission scan is therefore recommended for all infants admitted to the NICU, as it may reveal clinically unsuspected findings even in the absence of overt neurological problems. For routine CUS scanning in preterm infants most NICUs follow a standardized protocol stratified by gestational age (GA) and risk for brain injury. For the most immature infants with a gestational age below 28 weeks, CUS scans on day 1, 3, 7, 14, 21, 28 and then every other week until discharge or term equivalent age are recommended (1). Serial scanning will ensure that the most common types of preterm brain pathologies (congenital abnormalities, intraventricular hemorrhage, venous infarction, ventriculomegaly, cystic and non-cystic white matter injury) will be detected (2, 3). In more mature infants (GA 28-33 weeks) with an uncomplicated course CUS scans can be limited to day 1, 3, 7, 14, 28, six weeks, and term-equivalent age. In uncomplicated late preterm infants (GA 34-36 weeks) a single admission scan might be sufficient (1).

Brain Anatomy and Acoustic Windows

In neonates and young infants, the anterior fontanelle is the most commonly used acoustic window to perform CUS. However, the growing use of alternative acoustic windows —

including the mastoid and posterior fontanelles, the temporal and the foramen magnum view—has enhanced the quality of CUS brain imaging and expanded the range of detectable brain abnormalities (1, 4).

Anterior Fontanelle: Anatomy and Standard Planes

CUS is most commonly performed through the **anterior fontanelle** located at the junction between the two frontal and parietal bones. The anterior fontanelle is the largest and easiest accessible acoustic window within the first year of life, closing at an age of 12-18 months (5). Standardized CUS scanning protocols are helpful to ensure complete brain coverage, even in the presence of pathologies, and facilitate the review of CUS examinations by others. All relevant brain structures should be visualized in at least 2 planes in order to exclude artifacts. The examination should begin in the coronal plane, as this immediately reveals midline shifts and other asymmetric findings (1).

The transducer should be carefully placed on the fontanelle with a sufficient amount of warmed ultrasound gel. The marker of the ultrasound probe should point to the right, thereby the right hemisphere is displayed on the left side of the screen (1). The optimal acoustic window is found by gently sliding the transducer back and forth across the fontanelle, never compressing the superior sagittal sinus located beneath the anterior fontanelle. The probe is tilted anteriorly and posteriorly to scan the brain from the frontal lobes to the posterior parietal and occipital lobes. Symmetrical imaging is essential for reliable interpretation. To obtain sagittal and parasagittal images, turn the transducer 90 degrees until the marker points to the front and the front of the brain is displayed on the left side of the screen (1). The probe is tilted from the midline plane first to the right parasagittal brain surface and then to the left parasagittal brain surface marking the visualized brain side (1). Although there is no international consensus or evidence-based standard for documentation purposes, most experts recommend saving 6 images in the coronal plane (Figure 5) and 5 images in the sagittal plane (Figure 6) (1, 6). However, the exact planes vary from author to author. Nevertheless, by documenting “standard planes” it should not be missed to scan the whole brain. Pathological findings should always be documented in at least two different planes (1, 6). Preferably a cine clip visualizing the pathological finding should be recorded to facilitate the review by others.

Cerebral gyri and sulci serve as anatomical landmarks to identify the different lobes of the brain for adequate lesion localization. These include the central sulcus, which separates the frontal and parietal lobes, and the parietooccipital sulcus, which divides the parietal and occipital lobes (Figure 7-18). The lateral fissures allow easy identification of the temporal lobes. Using the anterior fontanelle as an acoustic window, the telencephalon is mainly represented by the frontal lobes, and the structures of the occiput and posterior fossa are difficult to assess with this approach alone.

Figure 5 Standard coronal planes obtained through the anterior fontanelle. Upper image: schematic illustration of the transducer on the anterior fontanelle with six dotted lines indicating the standard tilt positions from anterior (left) to posterior (right). Lower images: the six corresponding coronal planes. Middle row (planes 1–3, left to right): anterior planes at the level of the frontal lobes, the cavum septi pellucidi, and the foramina of Monro. Bottom row (planes 4–6, left to right): posterior planes at the level of the thalami including the posterior fossa, the atria of the lateral ventricles, and the temporal and occipital lobes.

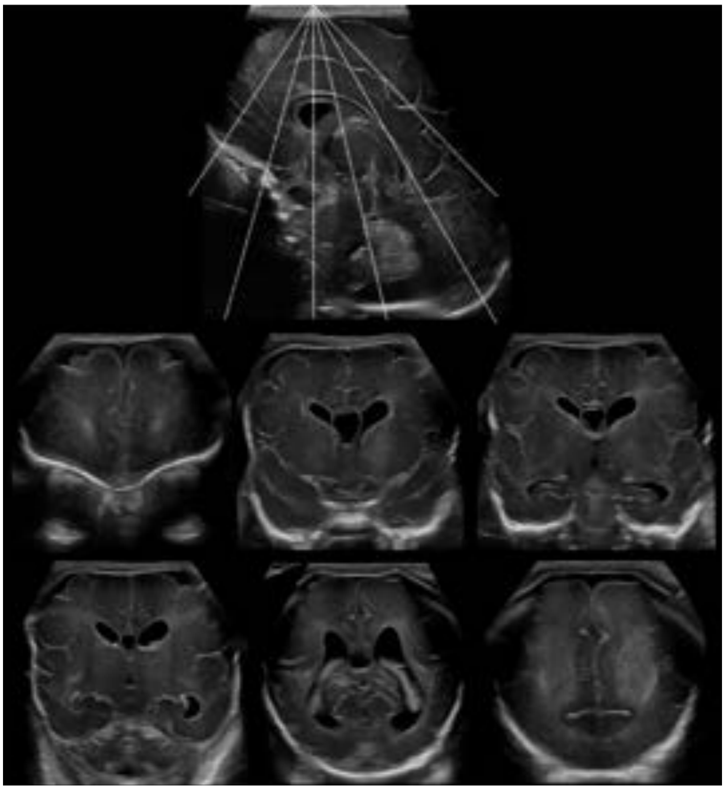

Figure 6 Standard sagittal planes obtained through the anterior fontanelle. Upper image: schematic illustration of the transducer on the anterior fontanelle with three dotted lines indicating the tilt positions to the median sagittal plane (vertical line) and to the left and right parasagittal planes (oblique lines). Lower images (left to right): median sagittal plane showing the corpus callosum, cerebellar vermis, and third ventricle (left); parasagittal plane through the deep grey matter showing the thalamus, basal ganglia, and choroid plexus (middle); parasagittal plane through the insula and brain surface showing the Sylvian fissure and cortical gyration (right).

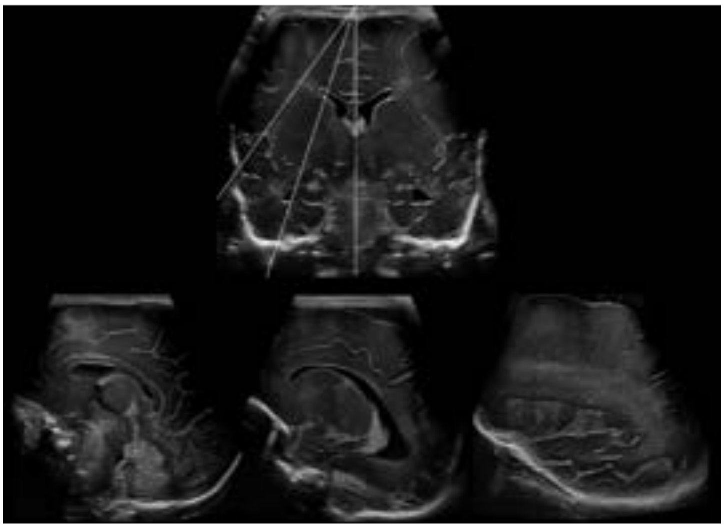

Figure 7 Anterior coronal planes around the level of the sulcus olfactorius. Three consecutive coronal planes from the most anterior (left) to a slightly more posterior position (right), demonstrating key anatomical landmarks of the anterior brain. The interhemispheric fissure (1), cingulate sulcus (3), corpus callosum (4), and anterior horns of the lateral ventricles (5) are visible in the midline. Laterally, the olfactory sulcus (6) and lateral fissure (7) demarcate the frontal and temporal lobes (8). In the most anterior plane (left image), the orbita (2) are visible inferiorly.

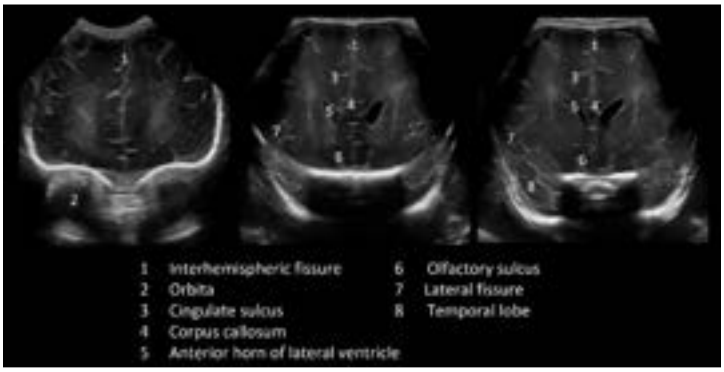

Figure 8 Coronal planes around the level of the foramina of Monro. Three consecutive coronal planes at the level of the foramina of Monro (left to right: from anterior to posterior), demonstrating key midline and deep structures. In the midline, the interhemispheric fissure (1), cingulate sulcus (4), corpus callosum (5), cavum septi pellucidi with septum pellucidum (7), and anterior horns of the lateral ventricles (6) are visible. The foramina of Monro (9), third ventricle (11), and tela choroidea (10) become visible in the more posterior planes. Laterally, the lateral fissure (2) and temporal lobes (3) are demonstrated, with the temporal horns of the lateral

ventricles (13) and cisterna interpeduncularis (12) visible inferiorly. The os sphenoidale/sella turcica (8) serves as an inferior bony landmark.

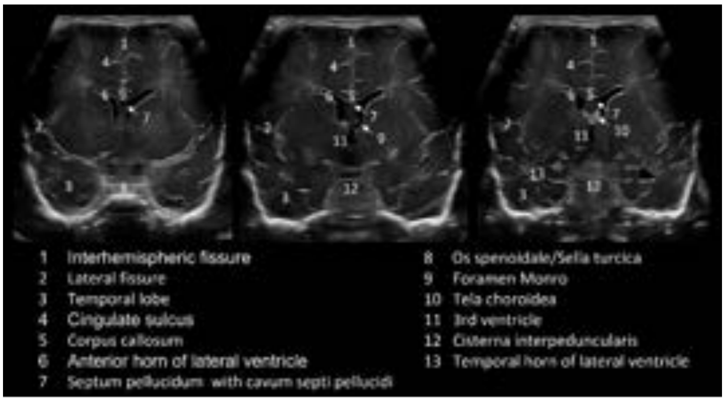

Figure 9 **Deep grey matter anatomy in an extremely preterm infant. Four coronal planes at the level of the basal ganglia demonstrating the deep grey matter structures in a very preterm infant. The caudate head (1), putamen (2), pallidum (3), and thalamus (6) are shown with their characteristic echogenicity pattern, which is notably higher in preterm infants than at term. The anterior (4) and posterior (7) limbs of the internal capsule appear as hypoechoic bands separating the basal ganglia. The anterior commissure (5) is visible in the midline in the intermediate planes.**

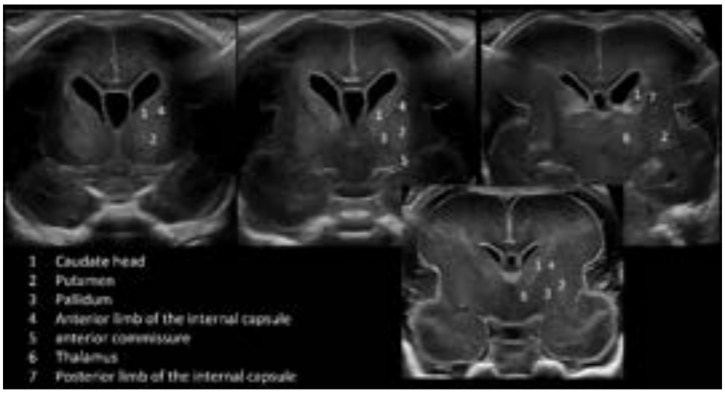

Figure 10 **Coronal planes through the thalamus. Three consecutive coronal planes at the level of the thalami, progressing from anterior (left) to posterior (right). The interhemispheric fissure (1), lateral fissure (2), insula (3), corpus callosum (4), and choroid plexus (5) are visible in the midline and paramedian regions. The thalami (6) are the dominant deep grey matter structures at this level; the posterior limb of the internal capsule (7) separates them from the basal ganglia.**

The most posterior plane (right image) includes the cerebral peduncles (8), fourth ventricle (9), cerebellar hemispheres (10), and cerebellar vermis (11).

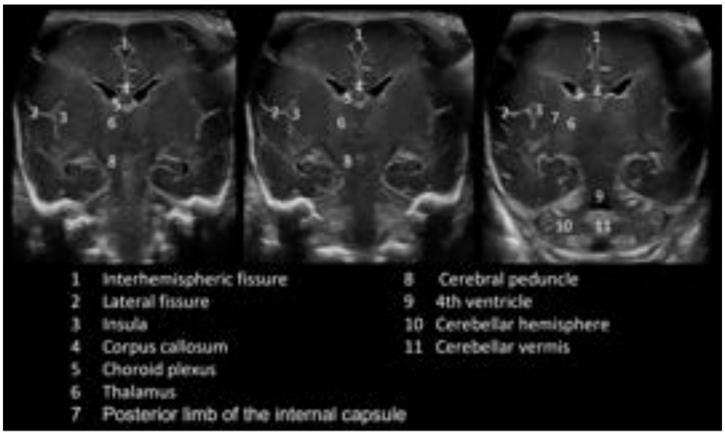

Figure 11 **Coronal planes through the atria of the lateral ventricles. Three consecutive coronal planes at the level of the ventricular atria, progressing from anterior (left) to posterior (right). The corpus callosum (3), cavum vergae (4) and choroid plexus (5) are visible in the midline; the lateral fissure (2) serves as lateral landmarks. The optic radiations (8) form echogenic bands lateral to the ventricular atria, and the calcar avis (9) is identifiable as an indentation on the medial ventricular wall. The thalami (6) and cerebellum (7) are visible in the more anterior planes.**

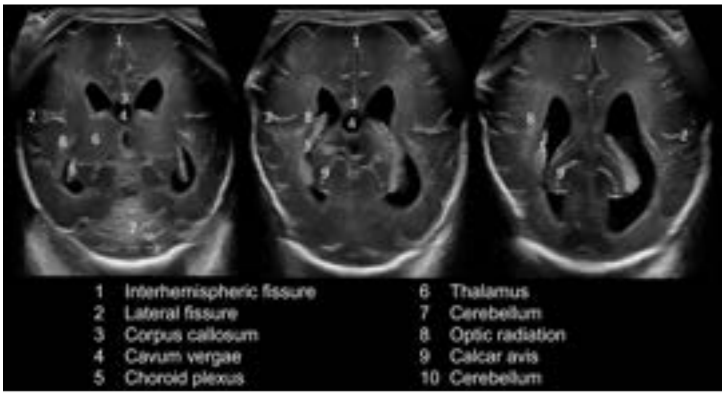

Figure 12 **Coronal planes through the brain surface. Three consecutive coronal planes at the level of the parietal and occipital cortex, progressing from anterior (left) to posterior (right), demonstrating the cortical sulcal anatomy. Key landmarks visible on the medial surface include the parietooccipital sulcus (3) and calcarine sulcus (4), which together form the characteristic Y-shaped configuration. On the lateral surface, the central sulcus (6), postcentral sulcus (7), and intraparietal sulcus (8) are identifiable. In the most posterior plane (right image), the superior**

precentral sulcus (5) and the ramus supramarginalis sulci cinguli (2) further delineate the parietal lobe anatomy.

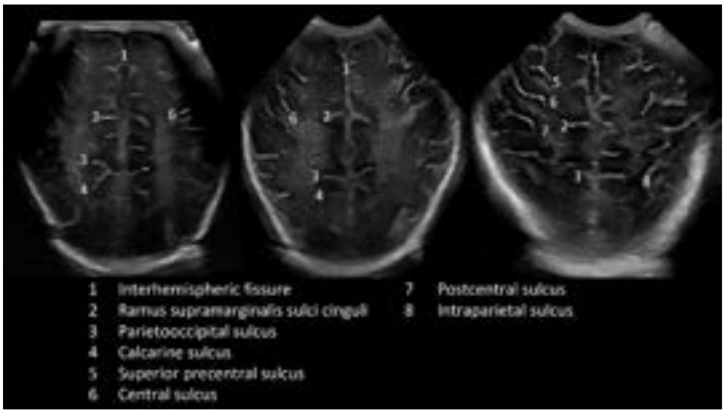

Figure 13 Median sagittal plane. Two median sagittal planes demonstrating the midline anatomy of the neonatal brain in a late preterm (left) and an extremely preterm infant (right). Key structures visible on the medial surface include the cingulate sulcus (1) and cingulate gyrus (3) above the corpus callosum (4), and the sulcus supramarginalis sulci cinguli (2) posteriorly. The choroid plexus (5) and foramen of Monro (6) mark the ventricular system. More inferiorly the mesencephalon (8), tectum (9), interpeduncular cistern (10), pons with basis pontis and tegmentum (11) are visible. In the posterior fossa the cerebellar vermis (12), and cisterna magna (13) are clearly delineated. The parietooccipital sulcus (7) separates the parietal from the occipital lobe (14).

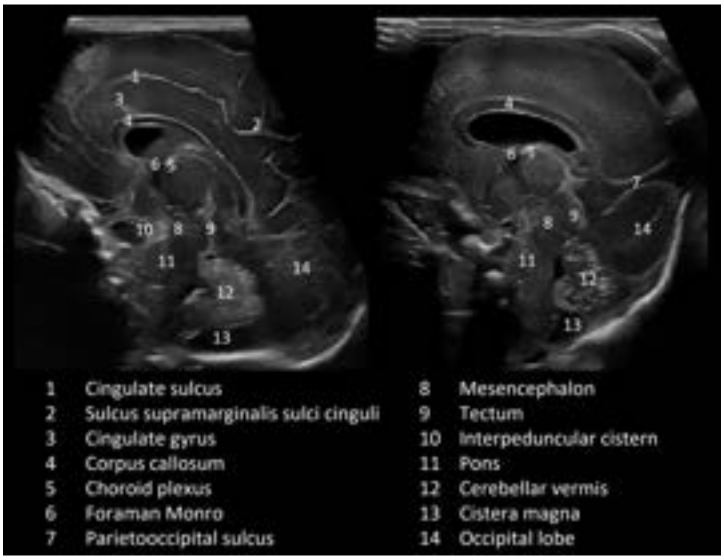

Figure 14 Parasagittal planes through the deep grey matter. Three parasagittal planes at increasing distance from the midline (left to right), demonstrating the deep grey matter structures and their relationships. In the more medial planes (left and middle images), the cingulate sulcus (1), cingulate gyrus (2), corpus callosum (3), caudate head (4), putamen (5), globus pallidum (6), choroid plexus (7), and thalamus (8) are identifiable. The parietooccipital (9) and calcarine sulci (10) are visible posteriorly. In the more lateral plane (right image), the medial temporal structures become prominent, including the parahippocampal gyrus (11), uncus with amygdala (12), pes hippocampi (13), and rhinal and collateral sulcus (14).

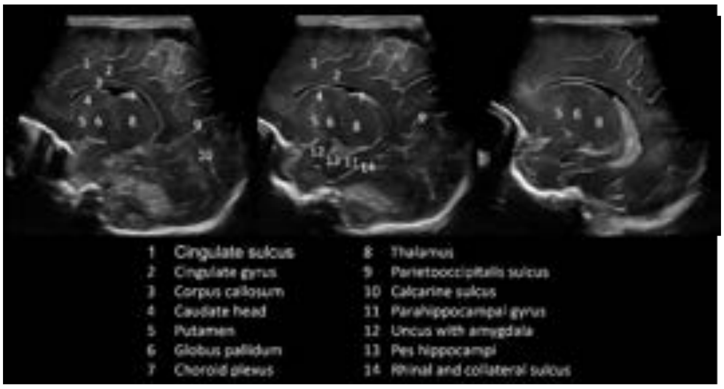

Figure 15 Deep grey matter anatomy in an extremely preterm infant. Two parasagittal planes through the basal ganglia in a very preterm infant, demonstrating the characteristically high echogenicity of the deep grey matter structures at this gestational age. The caudate head (1), putamen (2), pallidum (3), and thalamus (5) are clearly delineated, separated by the anterior (4) and posterior (6) limbs of the internal capsule. The medial temporal structures — uncus with amygdala (7) and hippocampus (8) — are visible in the left image. Note that the echogenicity of the striatum and thalamus is notably higher in preterm than in term infants.

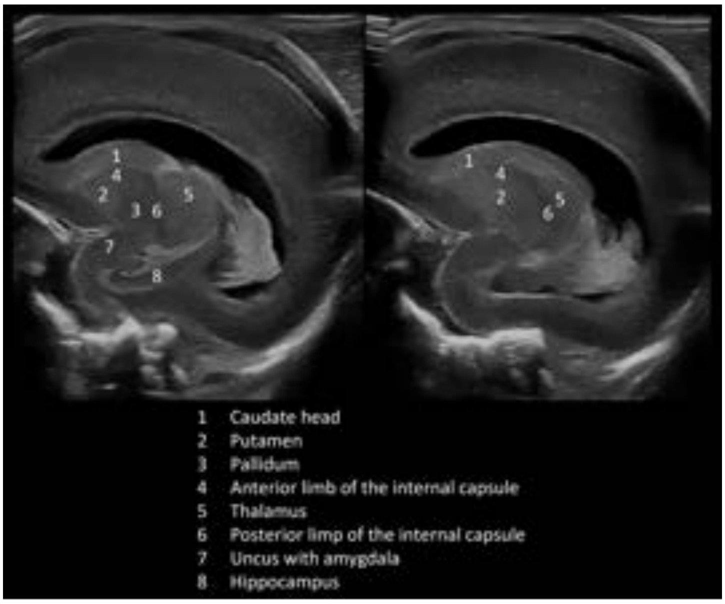

Figure 16 **Parasagittal planes through the insula. Three consecutive parasagittal planes through the insula at increasing distance from the midline (left to right). In the most medial plane (left image), the increased echogenicity due to white matter fibers (1) and open lateral fissure (2) are visible. As the plane moves laterally, the sulcus circularis insulae (3) becomes identifiable, demarcating the insular cortex from the surrounding opercula. In the most lateral plane (right image), the insula is increasingly covered and the central sulcus (4) becomes visible on the brain surface.**

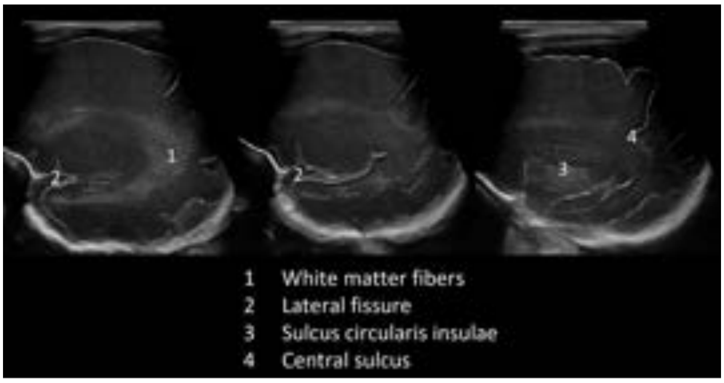

Figure 17 **Parasagittal plane through the insula at different gestational ages. Parasagittal plane through the insula in a term (left image) and preterm infant (right image), illustrating maturational differences in opercularization. In the term infant, the insula is fully covered by the frontal, parietal, and temporal opercula; the sulcus circularis insulae (1), individual insular sulci and gyri (3), and the central sulcus (2) are clearly identifiable. In the preterm infant, the lateral fissure (1) is wider**

and the insula remains partially exposed; importantly, the insular surface is smooth and flat, lacking the sulci and gyri that develop with advancing maturation.

Figure 18 Parasagittal plane through the brain surface. Three parasagittal planes at the level of the lateral brain surface, demonstrating the cortical sulcal anatomy of the frontoparietal region. The central sulcus (1) separates the frontal and parietal lobes and serves as the primary landmark at this level. The superior precentral sulcus (2) is visible anteriorly to the central sulcus, and the inferior precentral sulcus (3) further subdivides the precentral gyrus in the most lateral plane (right image). The postcentral sulcus (4) is identifiable posterior to the central sulcus, delineating the postcentral gyrus.

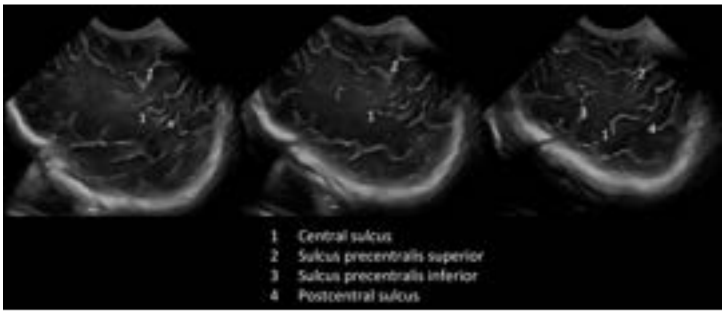

Additional Acoustic Windows: Anatomy and Planes

Additional acoustic windows include the posterior fontanelle (Figure 19), temporal view through sphenoid fontanelle/ temporal bone (Figure 20, 21), mastoid fontanelle (Figure 22), and foramen magnum (Figure 23). The use of complementary acoustic windows allows detecting lesions in otherwise hard-to-reach brain regions such as the parietal and occipital lobes, brainstem, and posterior fossa (Figure 24) (4).

The **posterior fontanelle** is much smaller than the anterior fontanelle. It is located between the occipital and parietal bones and closes at about two months of age in term born infants (6). Depending on its size and the degree of overlap of the cranial sutures, the ability to serve as an acoustic window varies remarkably. The posterior fontanelle is especially useful for visualizing the parietal and occipital lobes, the posterior horns of the lateral ventricles, midbrain and brainstem in coronal and sagittal planes (Figure 19).

Figure 19 Posterior fontanelle view in sagittal planes. Three sagittal planes obtained through the posterior fontanelle, from medial (left) to far parasagittal (right). The left image shows the median sagittal plane demonstrating the posterior cortical and deep anatomy, including the parietooccipital sulcus (1), cingulate gyrus (2), cingulate sulcus (3), corpus callosum (4), diencephalon (5), mesencephalon (6), pons (7), cerebellum (8), fourth ventricle (9), and medulla oblongata (10). The middle image shows an intermediate parasagittal plane at the level of the lateral ventricle (12) with the calcar avis (11), choroid plexus (13), and thalamus (14) clearly visible. The right image demonstrates a far parasagittal plane through the brain surface, providing a detailed view of the posterior parietal and occipital cortical gyration. Note the complementary visualization of posterior brain structures that are difficult to assess through the anterior fontanelle alone.

In the region around the ear, several acoustic windows can be used. The **sphenoid (or anterolateral) fontanelle** located between the sphenoidal, parietal, temporal and frontal bones, typically closes around six months of age. It transitions directly into the thin part of the temporal bone, which continues to serve as an acoustic window even after ossification - this is referred to as the **temporal acoustic window**. The temporal acoustic window allows a detailed visualization of the temporal lobes, diencephalon, midbrain, and brainstem, as well as the third ventricle, aqueduct and the Circle of Willis (Figure 20, 21). Color and pulsed-wave Doppler through this acoustic window allow assessment of the anterior, middle, and posterior cerebral arteries, including flow velocities and resistive indices, and remain feasible even after closure of the anterior fontanelle. The **mastoid (or posterolateral) fontanelle** located between the temporal, parietal and occipital bones typically closes between 6 and 18 months of age (7). The mastoid fontanelle is particularly useful for evaluation of the posterior fossa (Figure 22) (4, 7). For the temporal acoustic window, the transducer is placed in front of the ear, and for the mastoid-fontanelle window, the transducer is placed behind the ear, gently adjusting the position while searching for the best acoustic window. Both acoustic windows enable visualization of intracranial structures in coronal and axial planes. In axial planes, the cerebrum appears on the left side of the screen, while the cerebellum is displayed on the right.

With the head gently tilted forward (chin to chest), the foramen magnum can be used as an acoustic window to visualize the posterior fossa, the brainstem and spinal cord (Figure 23) in sagittal and axial planes (8, 9).

Figure 20 **Temporal acoustic window in axial planes. Two axial planes obtained through the temporal acoustic window at slightly different levels. In both planes, the cerebrum is displayed on the left and the cerebellum on the right of the screen. Key structures visible include the cerebellar hemispheres (1), cerebellar vermis (2), fourth ventricle (3), midbrain (4), temporal lobes (5), and temporal horns of the lateral ventricles (6) and insula (10). The deep grey matter structures (7) are well delineated in the more superior plane (right image), which additionally demonstrates the frontal horns of the lateral ventricles (8), and third ventricle (9).**

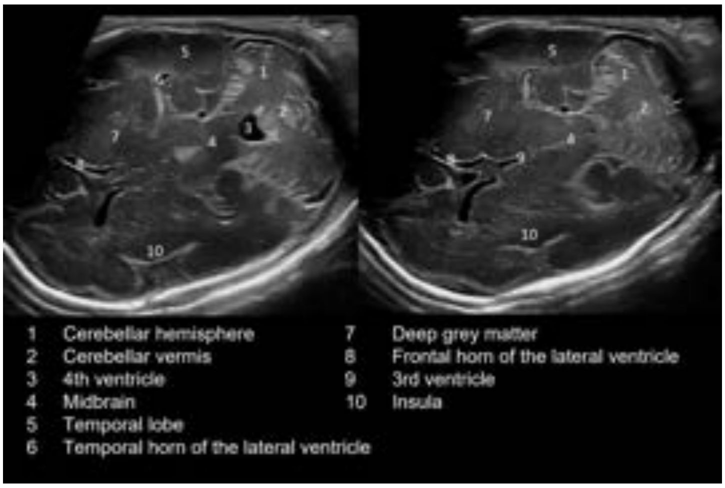

Figure 21 **Temporal acoustic window with deep grey matter anatomy in axial planes in an extremely preterm infant. Two axial planes through the temporal acoustic window at the level of the basal ganglia in a very preterm infant, providing high-resolution visualization of the deep grey matter. The left image demonstrates the caudate head (1), putamen (2), pallidum (3), anterior limb of the internal**

capsule (4), and posterior limb of the internal capsule (5) in detail. The right image shows a slightly different plane in which the anterior commissure (6) becomes visible as a thin hyperechoic band crossing the midline. Note the characteristically high echogenicity of the striatum typical for this gestational age. The temporal acoustic window is particularly suited for detailed evaluation of these structures due to its favorable angle of insonation.

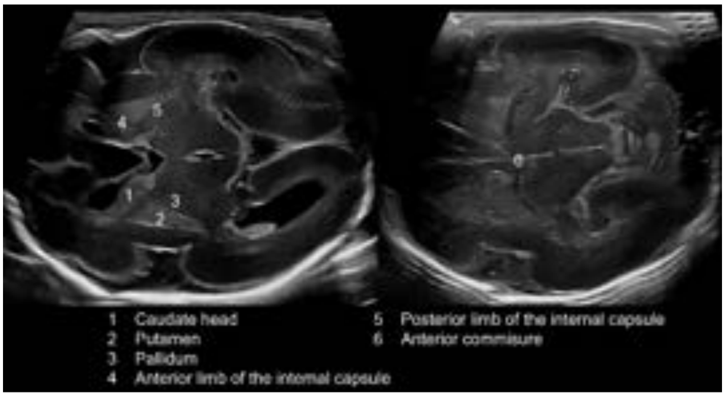

Figure 22 **Mastoid view. Two coronal planes obtained through the mastoid fontanelle at different levels. The left image shows a more inferior plane demonstrating both cerebellar hemispheres (1), the cerebellar vermis (2), fourth ventricle (3), and cerebral peduncles (4); the temporal lobe (5) is visible superiorly. The right image shows a more superior plane at the level of the vermis, where both cerebellar hemispheres (1) and the vermis (2) are displayed in closer proximity. The mastoid fontanelle view is the preferred acoustic window for evaluation of the posterior fossa and detection of cerebellar pathology.**

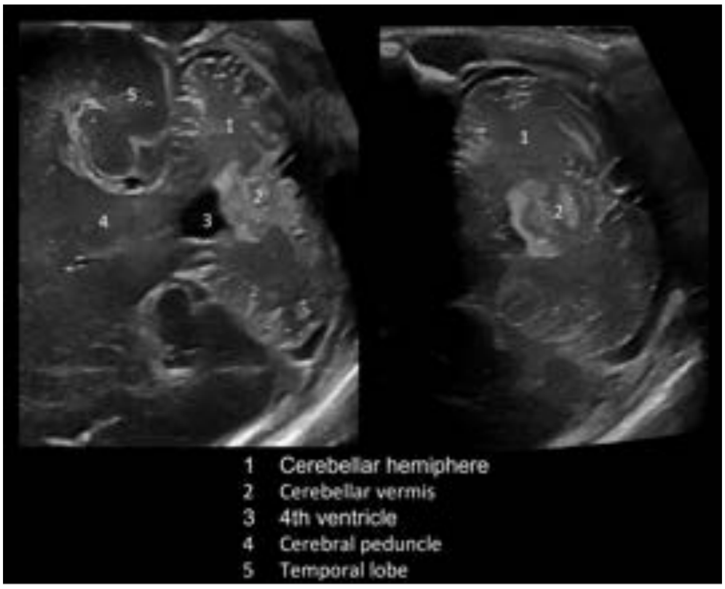

Figure 23 Foramen magnum view. Axial (left image) and sagittal (right image) planes obtained through the foramen magnum with the head gently tilted forward. The axial plane demonstrates the cerebellar hemispheres (1), cerebellar vermis (2), fourth ventricle (3), mesencephalon (4), and temporal lobes (5). The sagittal plane provides a unique longitudinal view of the posterior fossa and craniocervical junction, clearly delineating the pons (6), cisterna magna (7), medulla oblongata (8), and the proximal spinal cord (9). This acoustic window is particularly valuable for assessing brainstem morphology and the craniocervical junction.

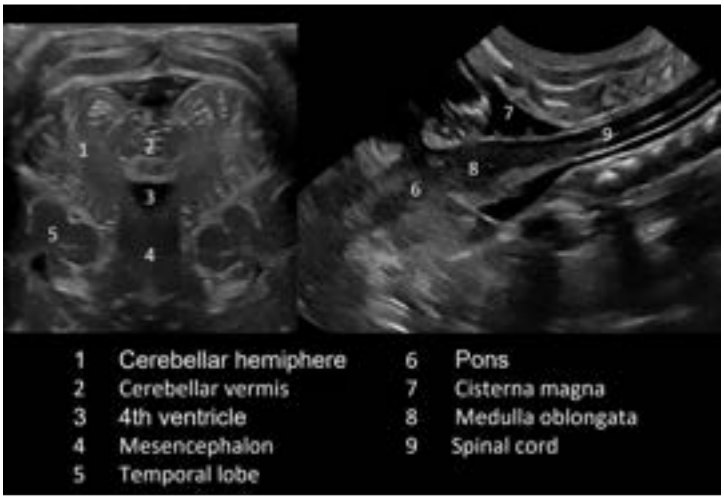

Figure 24 Detection of pathologies using alternative acoustic windows. Upper row: Visualization of a small parenchymal hemorrhage (3) in the parietal lobe adjacent to a subdural hemorrhage (2) — seen in a parasagittal plane through the anterior fontanelle (middle image) and confirmed in a coronal plane through the posterior fontanelle (right image); the central sulcus (1) serves as a cortical landmark. Lower row: Visualization of cystic ischemic damage in the occipital lobes through the posterior fontanelle in coronal planes at three levels, demonstrating the mesencephalon (4), fourth ventricle (5), and cerebellum (6) in progressively more posterior planes. Blood clots in the posterior horns of the lateral ventricles are indicated by asterisks. These cases illustrate how alternative acoustic windows allow detection of lesions that are not or only partially visible through the anterior fontanelle alone.

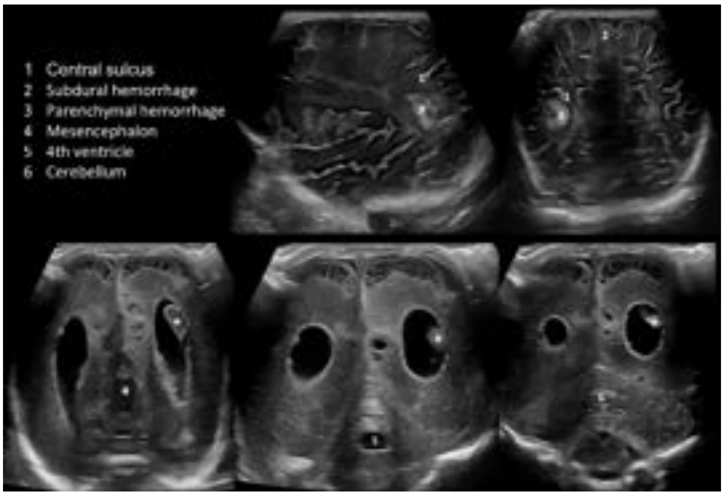

Immature Brain Characteristics

The neonatal brain — particularly in preterm infants — differs markedly from the mature brain in its structural appearance on CUS, reflecting the rapid functional, histologic, and anatomic changes occurring during fetal and early postnatal development. Constant brain growth and an increase in cortical folding, following a predetermined program, are associated with a significant increase in brain surface area (8).

Regional gyrification follows a specific progression (8). The medial surfaces (calcarine, cingulate, and parietooccipital sulci) develop first, followed by the central regions (central, precentral, and postcentral sulci), and then the lateral surfaces (Sylvian fissure and superior temporal sulcus). Lastly, the association areas (prefrontal and temporo-parietal) evolve (8). Around 20 weeks of gestation, the calcarine sulci (marking the location of the primary visual cortex) and parietooccipital sulci (separating the occipital and parietal lobes) become detectable (9). The cingulate and collateral sulci, which demarcate the limbic system — the cingulate sulcus forming its superomedial boundary above the cingulate gyrus, and the collateral sulcus its inferotemporal boundary below the parahippocampal gyrus — appear around 20–25 weeks (8). The central sulci become clearly detectable by 24–25 weeks, separating the parietal and frontal lobes (1). However, at 24 weeks of gestation the brain surface appears smooth on CUS and the lateral fissure is wide open (Figure 25, 26). The olfactory sulci become sonographically detectable in the late second trimester, followed by the pre- and postcentral sulci (27–29 weeks) (1, 8). Around 28 weeks, the superior temporal sulci (emerging posteriorly at 26 weeks and extending anteriorly by 30 weeks) and the secondary sulci (parietal and temporal before frontal) begin to develop (1, 8). From the 32nd week of gestation, the precentral and postcentral sulci branch out and the superior frontal sulci become evident (1, 8).

Alongside gyrification, opercularization of the insula follows a separate but parallel maturational timeline. Opercularization begins around 20–24 weeks in its posterior part. By 31 weeks, the middle operculum is completely closed and the insula is therefore covered by the frontal, parietal, and temporal lobes in the coronal plane at the level of the interventricular foramen of Monro (10). The entire opercularization process is complete by term.

CUS can reliably monitor the progression of cortical maturation and detect associated pathologies (10). It should be noted that gyrification varies between individuals and between the right and left hemispheres (8), and that the gestational age at which a given sulcus first becomes detectable differs between anatomical studies, fetal MRI, and ultrasound — with imaging typically lagging behind anatomical dissection by approximately 1–2 weeks (1, 8).

Figure 25 **Immature gyration and opercularization in a preterm infant of 23 weeks of gestation in coronal planes. Six standard coronal planes from anterior (upper left) to posterior (lower right). The upper row shows the anterior planes: the brain surface appears smooth, the lateral fissure is wide open reflecting incomplete opercularization, and the insula is fully exposed. The lower row shows the more posterior planes, where the deep grey matter structures and posterior fossa become visible. Throughout all planes, the absence of cortical sulci and gyri reflects the characteristic lissencephalic appearance of the brain at this gestational age.**

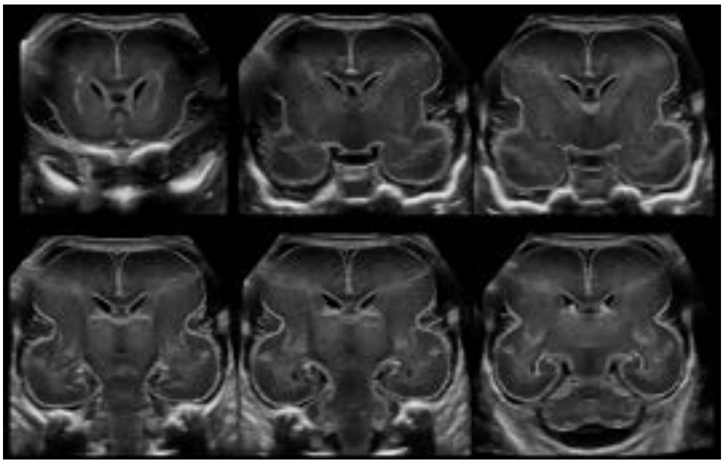

Figure 26 **Immature gyration and opercularization in a preterm infant of 23 weeks of gestation in sagittal and parasagittal planes. Six sagittal and parasagittal planes from medial (upper left) to far parasagittal (lower right). The median sagittal plane (upper left) demonstrates the corpus callosum and posterior fossa structures, including the cerebellar vermis. The parasagittal planes show the characteristically smooth, lissencephalic brain surface with an absence of**

cortical sulci and gyri. The lateral fissure is wide open throughout all planes and the insula is fully exposed, reflecting the incomplete opercularization at 23 weeks of gestation.

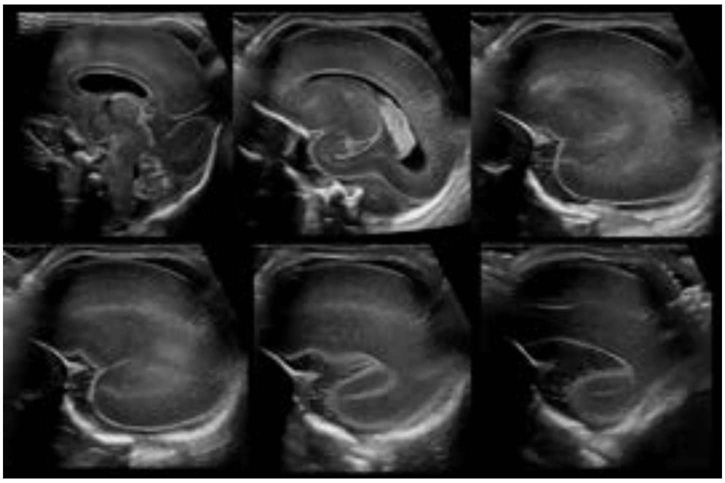

Identifying Brain Lesions

Familiarity with the normal echogenicity and echotexture of intracranial structures is the basis for recognizing pathological changes.

Cerebral cortex and white matter

Normal cortical differentiation on CUS is characterized by a distinct sequence of grey scale intensities. The pia mater, which covers the surface of the brain, appears hyperechogenic (bright or 'white'). Beneath it, moving from the outside inwards, the cortical grey matter appears hypoechoic ('dark grey'), followed by subcortical white matter of intermediate echogenicity ('grey'), with a smooth transition between grey and subcortical white matter (Figure 27). This typical pattern is altered by ischemic or other injuries. Affected structures may become more echogenic, resulting in an increased brightness of the grey matter in cases of cortical necrosis (Figure 28) or reduced echogenicity (‘darkening’) of the grey matter when the subcortical white matter is injured (Figure 29).

Figure 27 Normal cortical differentiation in a posterior coronal and a parasagittal plane. Two high-resolution CUS images demonstrating normal cortical differentiation in a term infant. In both planes, the characteristic three-layer pattern of the cortical ribbon is clearly visible: the pia mater appears as a thin hyperechogenic (bright) line on the brain surface, beneath which the cortical grey matter appears hypoechoic (dark), followed by the subcortical white matter of intermediate

echogenicity. This distinct layering is best appreciated at the walls and floors of the sulci, where the insonation angle is perpendicular to the cortical surface. The posterior coronal plane (left image) provides a symmetric overview of the cortical ribbon across multiple sulci, while the parasagittal plane (right image) demonstrates the layering in detail along the individual gyri and sulci of the frontal and parietal lobes.

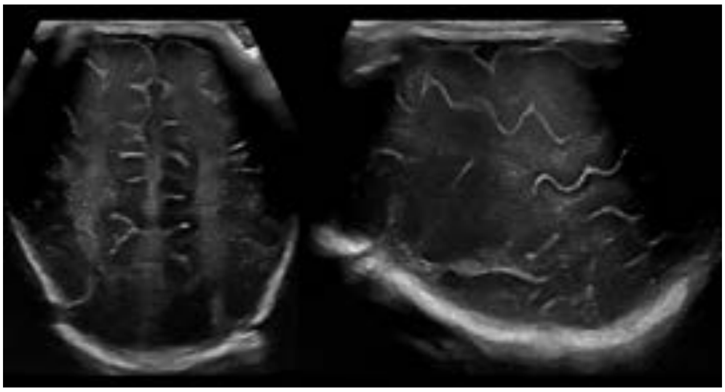

Figure 28 Loss of normal cortical differentiation in cortical necrosis. CUS images demonstrating abnormal cortical echogenicity due to different etiologies of ischemic injury. In all three planes, the normal three-layer cortical pattern is lost and the cortical grey matter appears markedly hyperechogenic, becoming indistinguishable from the underlying white matter. The two coronal planes (left and middle images) show diffuse bilateral cortical hyperechogenicity in a term infant with hypoxic-ischemic encephalopathy, reflecting widespread cortical necrosis. The parasagittal plane (right image) demonstrates focal cortical hyperechogenicity restricted to the territory of the middle cerebral artery in a term infant with perinatal arterial ischemic stroke (PAIS). In both conditions, the abnormal cortical brightness is best appreciated by comparison with the normal three-layer pattern shown in Figure 27.

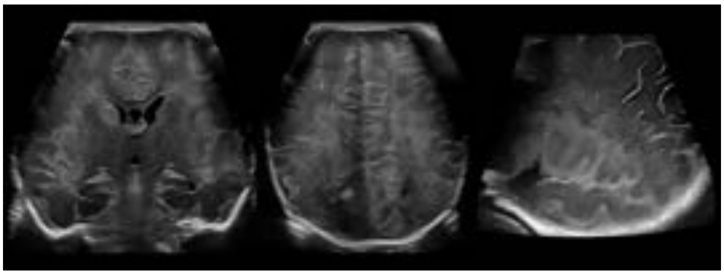

Figure 29 Progressive subcortical and diffuse white matter injury in hypoxic-ischemic encephalopathy. CUS images of a term infant with hypoxic-ischemic

encephalopathy, obtained on day of life (DOL) 5 (upper row) and DOL 7 (lower row), demonstrating the temporal evolution of white matter injury. On DOL 5 (upper row), a diffuse increase in echogenicity of the subcortical and deep white matter is already evident, while the cortical grey matter remains partially distinguishable. By DOL 7 (lower row), the white matter hyperechogenicity has markedly progressed, now affecting the subcortical white matter diffusely throughout both hemispheres with near-complete loss of the normal grey-white matter differentiation. This rapid progression of white matter echogenicity over a short time interval is characteristic of severe hypoxic-ischemic injury and underscores the importance of serial CUS examinations in the acute phase.

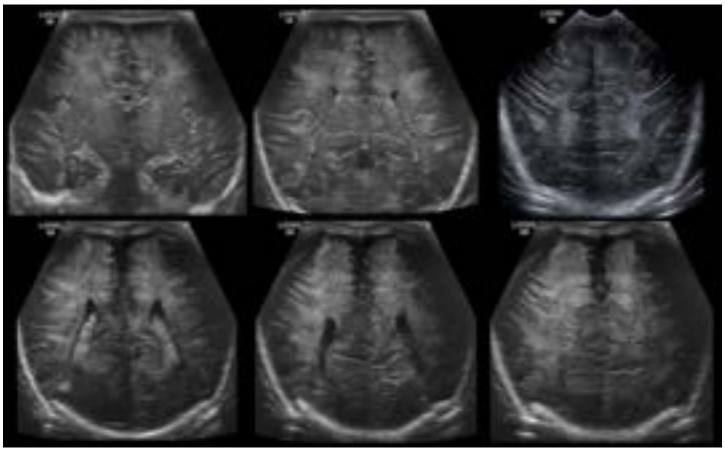

Figure 30 **Normal periventricular white matter hyperechogenicities. CUS images demonstrating physiological causes of increased periventricular echogenicity in preterm infants. The left image shows a focal area of increased echogenicity (arrow) corresponding to transitional fields or fiber tracts. The middle image demonstrates the echogenic optic radiation (arrowhead) along the ventricular wall. The right image shows the characteristic normal periventricular flaring (asterisk) caused by perpendicular angulation of the ultrasound beam to the periventricular white matter fibres (anisotropy). Recognition of these normal hyperechogenicities is essential to avoid misinterpretation as pathological white matter injury.**

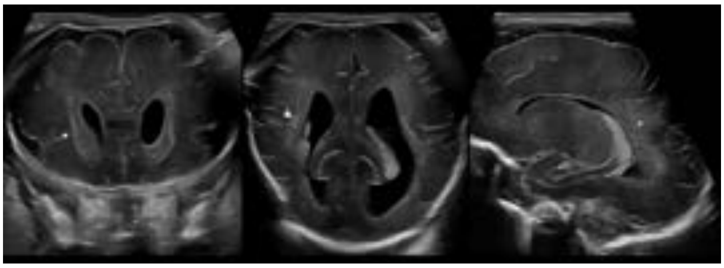

Figure 31 Normal and abnormal periventricular echogenicity in preterm infants. CUS images illustrating the spectrum from normal to pathological periventricular echogenicity, shown as coronal (upper row) and corresponding parasagittal (lower row) planes from three different patients. Left column: normal periventricular echogenicity in coronal and parasagittal planes. Middle column: homogeneously increased periventricular echogenicity (flaring) in coronal and parasagittal planes, representing a benign physiological finding. Right column: inhomogeneous, patchy periventricular echogenicity increase (clouded flaring) in coronal and parasagittal planes, representing a pathological finding indicative of white matter injury (WMI). The distinction between homogeneous flaring and inhomogeneous clouded flaring is of critical diagnostic importance, as the latter carries a significantly higher risk of relevant white matter injury.

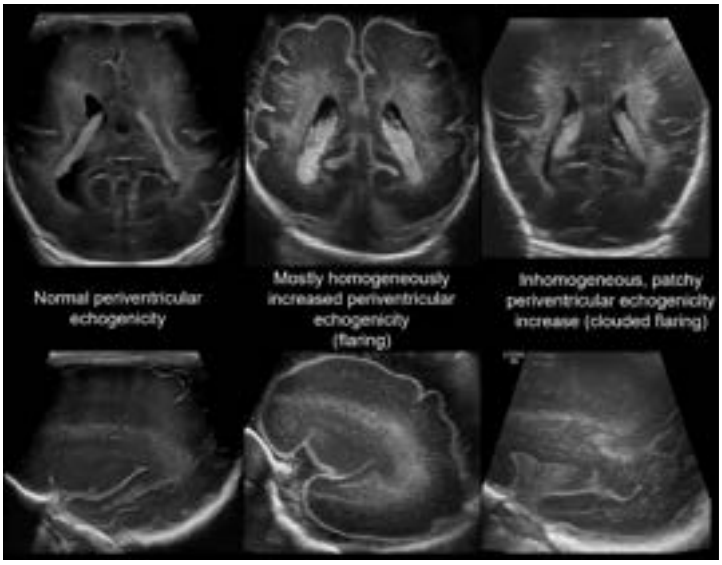

White matter shows mostly homogeneous intermediate echogenicity with areas of physiological increased echogenicity representing anatomical structures like migrating cells or white matter tracts (e.g. optic radiations). Normal, homogeneous periventricular hyperechogenicity is also caused by perpendicular angulation of the ultrasound beams to the periventricular white matter fibers (anisotropy) (Figure 30). The periventricular white matter is particularly vulnerable in preterm infants: immature pre-oligodendrocytes and arterial–venous border zones along the ventricles are highly susceptible to hypoxic-ischemic injury and to systemic inflammation (e.g. chorioamnionitis, sepsis, NEC), the two principal drivers of preterm white matter injury (WMI). A patchy increase in periventricular echogenicity with the absence of normal areas of hyperechogenicity is a pathologic finding typical for WMI (Figure 31) (2, 3). It may proceed to scarring (Figure 32), loss of white matter volume (Figure 33), and/or cystic degeneration (Figure 34) (2, 3). A similar pattern of periventricular hyperechogenicity can also be seen in term infants with hypoxic-ischemic injury; however, in term infants the injury typically extends beyond the periventricular region to involve the subcortical and deep white matter diffusely (Figure 29, 32) (11).

In contrast to patchy echogenicity (Figure 31), which represents inhomogeneous signal within otherwise solid parenchyma and may be seen both acutely and chronically (the latter reflecting gliotic scarring, as in punctate white matter lesions) (Figure 32), cysts appear as well-demarcated, anechoic (fluid-filled) cavities and always indicate a later stage of tissue loss (Figure 34). The typical finding in cystic WMI of prematurity is the presence of bilateral cysts in the periventricular white matter (Figure 34). These cysts usually develop within 2–4 weeks after the initial insult. In premature infants with cystic WMI the cysts often collapse and may disappear by term-equivalent age, leaving behind glial scarring and white matter volume loss, which can result in ventriculomegaly and enlarged subarachnoid spaces. Therefore, serial CUS examinations up to term age or discharge are crucial for detecting WMI of prematurity (1, 3).

In perinatal arterial ischemic stroke (PAIS) the increase in echogenicity corresponds to the affected vascular territory (Figure 35) (11, 12).

In case of venous congestion or venous periventricular hemorrhagic infarction the anatomy of the venous drainage pathways of the white matter causes a typical fan-shaped hyperechogenicity (Figure 36) (12). Hemorrhages are typically hyperechogenic with either rounded or irregular shape, and often space-occupying (Figure 36, 37) (11, 13).

Figure 32 **Non-cystic white matter injury. CUS images demonstrating non-cystic white matter injury (WMI) in two preterm infants. Left column: preterm infant born at 32 weeks of gestation, imaged at term-equivalent age. Two parasagittal planes (right and left hemisphere) show bilateral patchy areas of increased echogenicity in the periventricular and deep white matter, consistent with the chronic evolution of punctate white matter lesions (PWML). Right column: second patient with more severe non-cystic WMI showing markedly increased periventricular white matter echogenicity bilaterally in the coronal plane, accompanied by early ventricular enlargement and white matter volume loss; the parasagittal plane confirms the diffuse extent of the injury consistent with punctate white matter injury.**

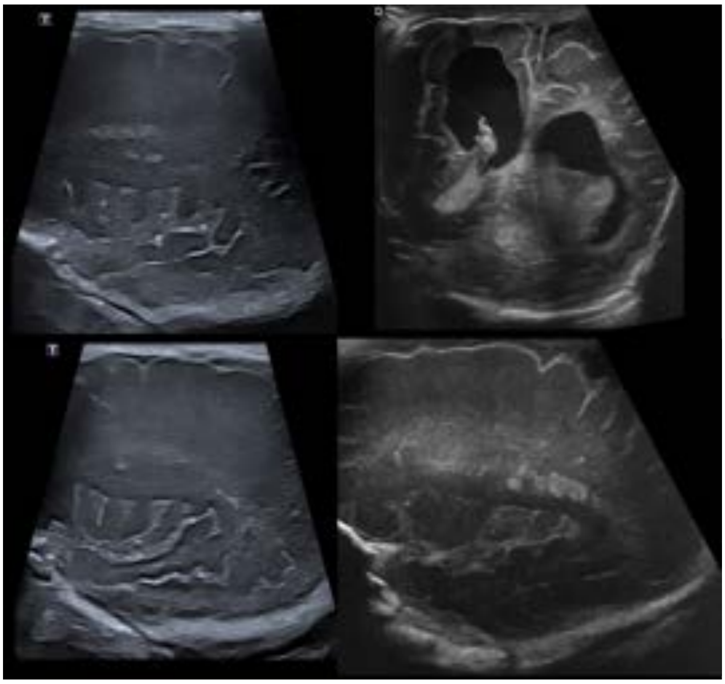

Figure 33 **White matter volume loss due to white matter injury. CUS images in coronal (upper row and lower left) and parasagittal (lower right) planes demonstrating the sequelae of white matter injury (WMI) in a preterm infant at 36 weeks of gestation. All planes show a markedly enlarged ventricular system with irregular margins and reduced periventricular white matter volume. The widened subarachnoid spaces and prominent cortical gyri further reflect the loss of white matter. The parasagittal plane (lower right) illustrates the characteristic elongated and irregular shape of the lateral ventricle resulting from the surrounding white matter volume loss. These findings represent the end-stage of severe WMI, in which the initial hyperechogenicity has resolved but left behind white matter volume loss and glial scarring. Serial CUS examinations up to term-equivalent age are therefore essential to detect this evolution.**

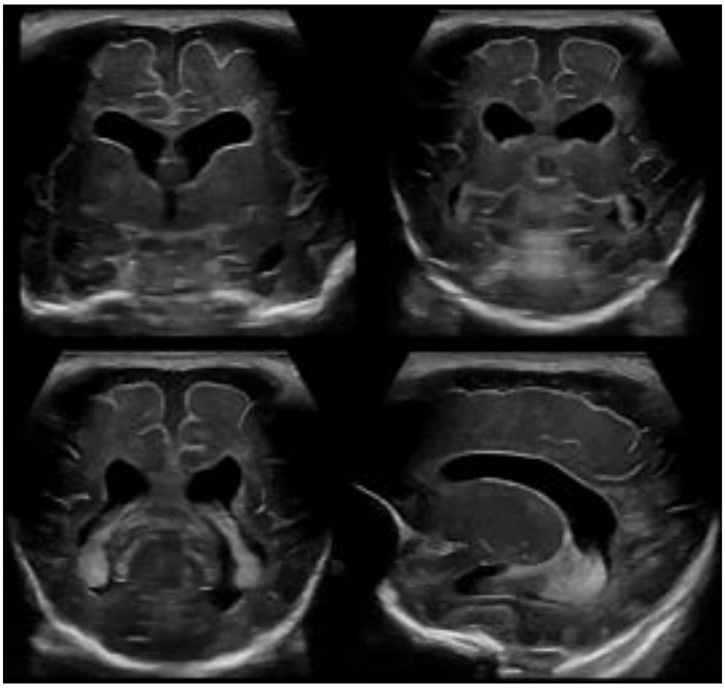

Figure 34 Cystic white matter injury. CUS images demonstrating cystic white matter injury (WMI) in two preterm infants. Left column: extremely preterm infant (23+4 weeks of gestation) following severe necrotizing enterocolitis (NEC). On day of life (DOL) 20, four days after the NEC episode (upper left), diffuse hyperechogenicity of the periventricular and subcortical white matter is evident in a parasagittal plane. By DOL 35, 19 days after the NEC episode (lower left), the initial hyperechogenicity has evolved into extensive cystic degeneration throughout the white matter, reflecting the characteristic temporal progression of cystic WMI. Right column: preterm infant (30+0 weeks of gestation) on DOL 33 showing symmetrical periventricular cysts in two coronal planes (upper and middle right) and in a parasagittal plane (lower right), with the cysts located in their typical position adjacent to the lateral ventricles. Together, these cases illustrate both the temporal evolution from initial hyperechogenicity to cyst formation and the typical bilateral, symmetrical periventricular distribution of cystic WMI of prematurity.

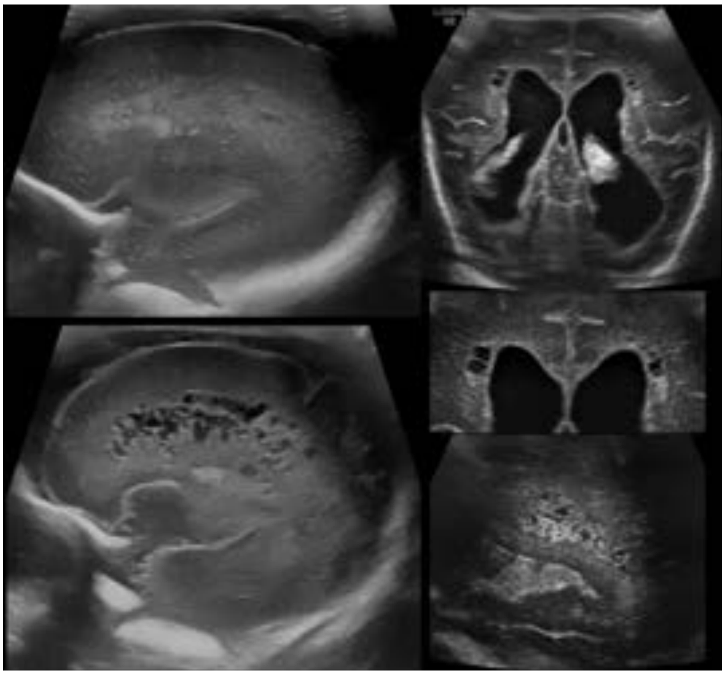

Figure 35 Perinatal arterial ischemic stroke in the territory of the left middle cerebral artery. Five CUS images in coronal (upper row) and parasagittal (lower row) planes demonstrating the typical echographic appearance of perinatal arterial ischemic stroke (PAIS) in the territory of the left middle cerebral artery (MCA). The hyperechogenicity corresponds precisely to the MCA territory, while the adjacent vascular territories — the anterior cerebral artery (ACA) territory along the medial hemisphere, the posterior cerebral artery (PCA) territory in the posterior and inferior regions, and the anterior choroidal artery (AChoA) territory — are spared and labeled for orientation. The coronal planes (upper row) demonstrate the asymmetric distribution of the hyperechogenicity, clearly delineated by the boundaries of the spared territories. The parasagittal planes (lower row) confirm the spatial extent of the infarction and its vascular territorial boundaries.

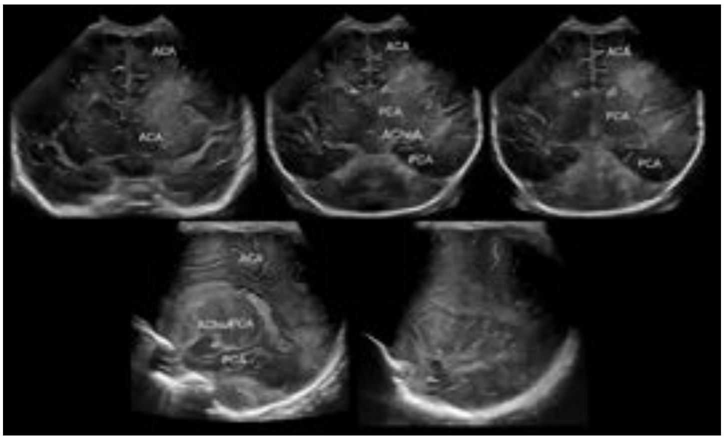

Figure 36 Parenchymal and thalamic hemorrhagic infarction in deep vein thrombosis. CUS images demonstrating the typical triad of deep cerebral vein thrombosis in a term infant. The coronal plane (upper left) shows bilateral thalamic hemorrhagic infarction and associated intraventricular hemorrhage, resulting from thrombosis of the internal cerebral veins and/or the vein of Galen. The three parasagittal planes (upper right, lower left, lower right) demonstrate the periventricular hemorrhagic infarction with its characteristic fan-shaped hyperechogenicity, reflecting occlusion of the medullary veins draining into the deep venous system, and illustrate its full spatial extent from different angles. The combination of periventricular hemorrhagic infarction, intraventricular hemorrhage, and thalamic hemorrhage constitutes the classical triad of deep cerebral vein thrombosis.

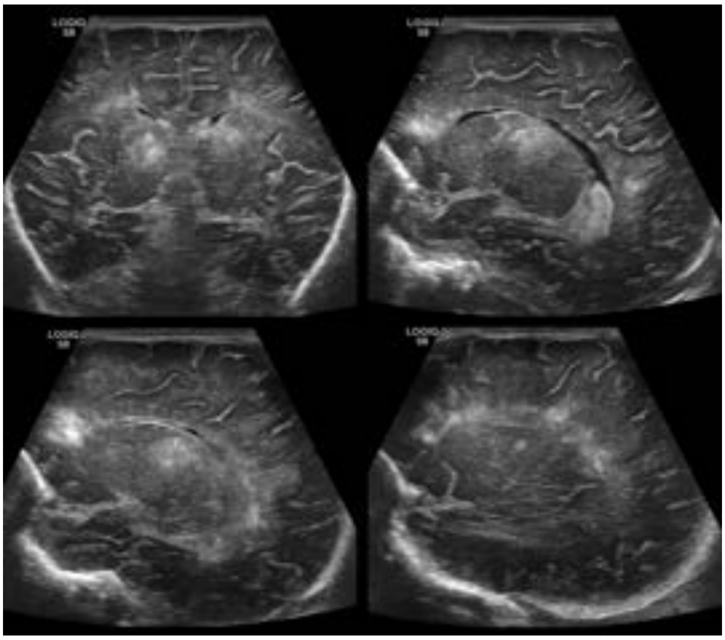

Figure 37 Intraventricular hemorrhage and periventricular hemorrhagic infarction with the typical fan-shaped appearance in preterm germinal matrix hemorrhage. CUS images demonstrating periventricular hemorrhagic infarction (PHI) in two preterm infants. The first patient (upper row and lower left) shows PHI resulting from occlusion of the caudate vein and medullary veins alongside the ventricle wall: the coronal plane (upper left) demonstrates intraventricular hemorrhage with ventricular dilatation and a large parenchymal hemorrhagic infarction, while the two parasagittal planes (upper right and lower left) clearly show the characteristic fan-shaped hyperechogenicity extending from the periventricular region into the white matter. The second patient (lower right) shows a terminal vein infarct in a parasagittal plane, with a more circumscribed fan-shaped

hyperechogenicity in the posterior periventricular region corresponding to the drainage territory of the terminal vein. The comparison of the two cases illustrates how the location and extent of the PHI depend on the specific occluded vein.

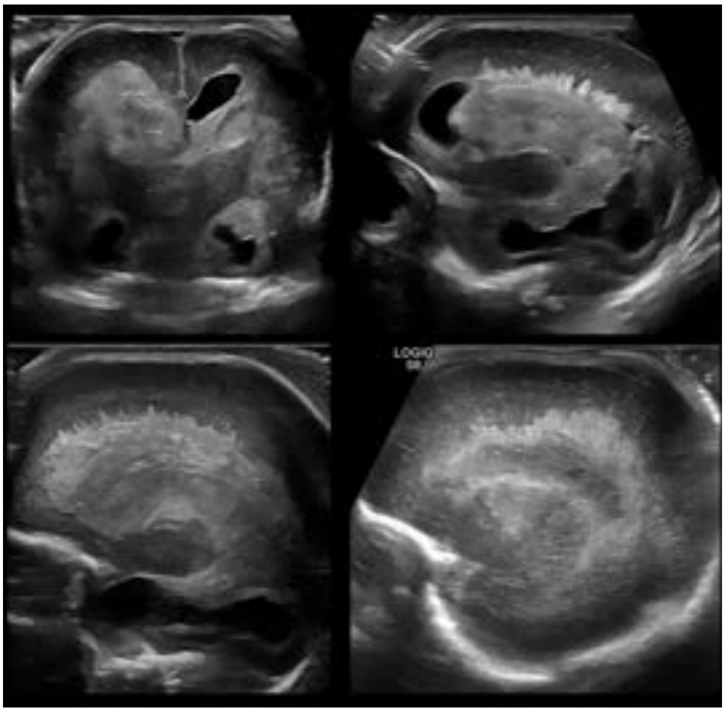

Deep grey matter

The structures of the deep grey matter have typical echogenicity patterns that vary with both gestational and postnatal age, with preterm infants showing higher echogenicity in the striatum and thalamus than term born infants (Figure 9, 15, 21) (14). Typical pathologic findings are associated with arterial ischemic stroke (Figure 35), especially perforator stroke (Figure 38), hypoxic ischemic injury (Figure 39, 40), hemorrhage (Figure 36), and cerebral infectious disease.

Figure 38 **Perforator stroke. Two parasagittal CUS images of the left hemisphere demonstrating a perforator stroke in a preterm infant. The greyscale image (left) shows a focal, well-demarcated hyperechogenic lesion in the region of the basal ganglia and internal capsule, corresponding to the territory of a single perforating artery. The color Doppler image (right) demonstrates preserved vascular flow in the adjacent vessels, confirming the focal nature of the infarction. Perforator strokes characteristically appear as small, rounded**

hyperechogenic lesions in the deep grey matter and are best visualized in the parasagittal plane.

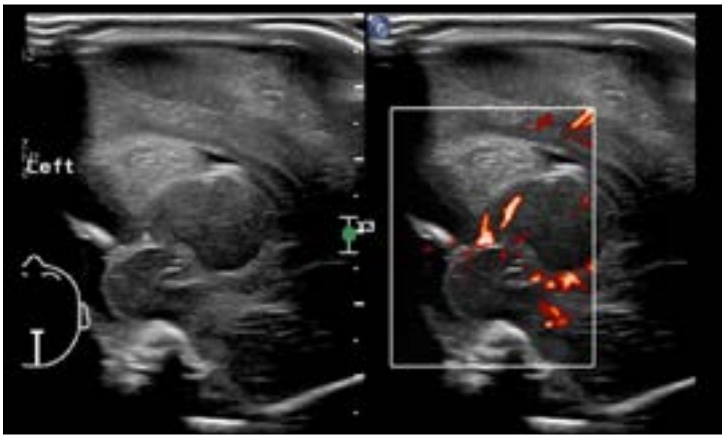

Figure 39 Bilateral thalamic hyperechogenicity after perinatal asphyxia. CUS images in coronal (upper row) and parasagittal (lower row, right and left hemispheres) planes demonstrating bilateral increased echogenicity of the thalami in a term infant following hypoxic-ischemic encephalopathy. The three coronal planes (upper row) show thalamic involvement at different levels, with symmetric hyperechogenicity of both thalami and loss of the normal thalamic echotexture. The parasagittal planes of the right (lower left) and left (lower right) hemispheres confirm the bilateral and symmetric distribution of the thalamic injury. Thalamic hyperechogenicity is a characteristic finding of severe hypoxic-ischemic injury and is associated with a poor neurodevelopmental outcome.

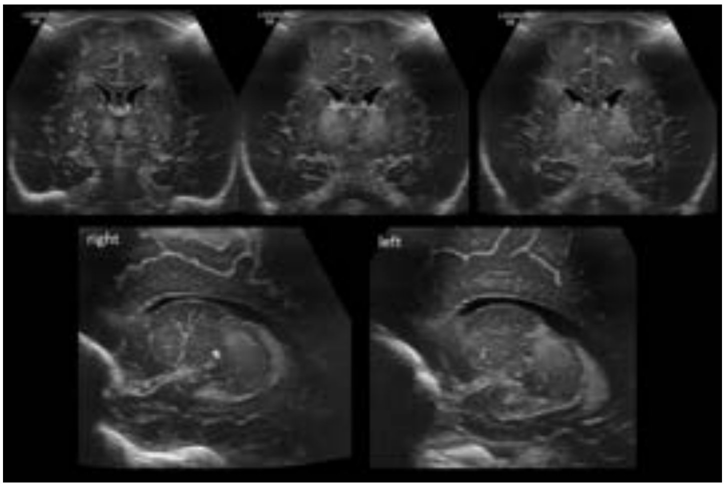

Figure 40 Increased echogenicity of the cortical, subcortical and deep grey matter after perinatal asphyxia. CUS images in coronal (upper row) and parasagittal (lower row) planes demonstrating diffuse hyperechogenicity of the cortex, subcortical

white matter, and deep grey matter structures in a term infant with severe hypoxic-ischemic encephalopathy. The two coronal planes (upper row) show diffuse bilateral increased echogenicity involving the cortical ribbon, subcortical white matter, and basal ganglia and thalami, producing the characteristic "four-column sign" in which the echogenic basal ganglia and thalami appear as four distinct hyperechogenic columns separated by the posterior limb of the internal capsule (PLIC). The PLIC is relatively spared, appearing as a hypoechoic band between the echogenic thalamus and basal ganglia. In addition, a focal hemorrhagic infarction into the injured white matter is visible on the right side, appearing as a markedly hyperechogenic lesion with posterior acoustic shadowing, superimposed on the diffuse white matter injury. The three parasagittal planes (lower row) confirm the extensive bilateral distribution and demonstrate an increased echogenicity of all structures of the deep grey matter separated by the hypoechogenic internal capsule. This pattern of diffuse injury is characteristic of the most severe forms of hypoxic-ischemic encephalopathy.

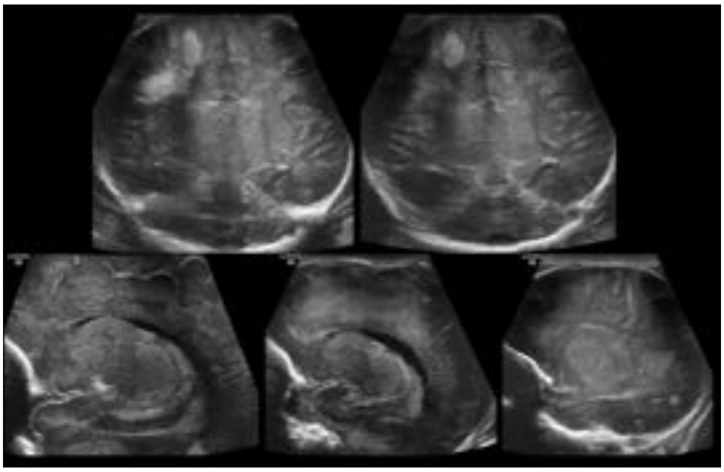

External cerebrospinal fluid spaces

The external cerebrospinal fluid (CSF) spaces consist of the three layers of the meninges (dura mater, arachnoid mater, and pia mater) and the spaces between them. The subarachnoid space, which is located between the pia and the arachnoid mater, contains CSF, blood vessels, and connective tissue (15). Therefore, on ultrasound, the subarachnoid space is not completely echo-free. The external CSF spaces should be assessed using a standardized approach. For quantification, the measurement of the sino-cortical and cranio-cortical distance is recommended (Figure 41) (16-18). Normal values depend on gender and age (Reference values: cranio-cortical distance (CCD): <4 mm; sino-cortical distances (SCD): <3 mm) (17, 18). It is essential to take measurements at a minimum of three different locations, such as the frontal, parietal, and occipital regions (16). A mild to moderate isolated enlargement in a single location—most commonly in the frontal region—is typically related to head shape. This is a frequent benign finding in preterm infants, who often exhibit a characteristic long, narrow head shape. After birth trauma or other trauma subdural and subarachnoid hemorrhage can be detected in the external cerebrospinal fluid spaces. In bacterial CSF infections, hyperechoic thickened meninges, empyema, and subdural collections can be found (Figure 41). High-frequency linear probes are particularly effective in detecting these abnormalities.

Figure 41 External cerebrospinal fluid spaces. CUS images demonstrating normal and pathological findings of the external cerebrospinal fluid spaces. Upper left: coronal plane in an extremely preterm infant with physiologically widened external CSF spaces, illustrating the standardized measurement of the cranio-cortical distance (CCD) and the sino-cortical distance (SCD). The widening is a benign finding in this age group, related to the characteristic elongated head shape of preterm infants. Upper right: high-frequency linear probe image in a term infant with abusive head trauma (shaken baby syndrome), showing bilateral subdural and subarachnoid hemorrhage; the arrows indicate the arachnoid membrane, which serves as the boundary between the subdural and subarachnoid compartments and is clearly delineated by the surrounding hemorrhage. Lower row: two coronal planes obtained with a high-frequency linear probe in an infant with bacterial meningitis, demonstrating markedly thickened and hyperechogenic meninges covering both hemispheres. High-frequency linear probes are essential for the detailed visualization of these superficial pathologies.

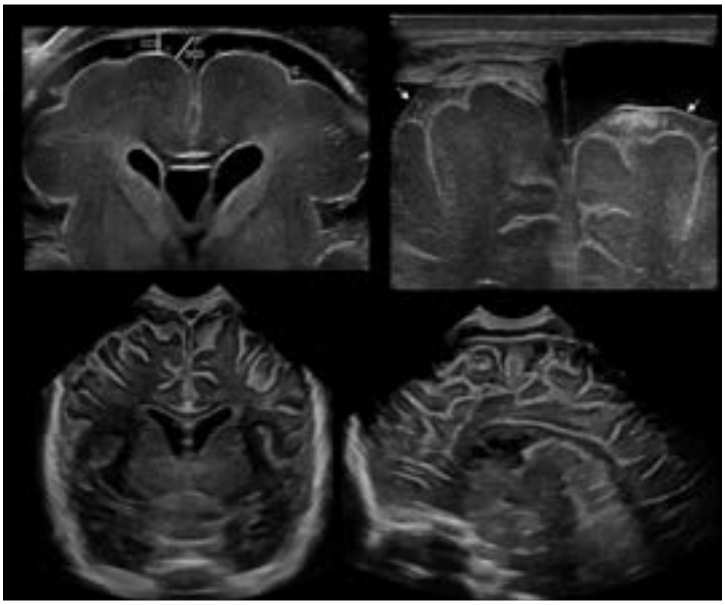

Ventricular system

The lateral ventricles and the 3rd and 4th ventricle can be easily visualized from the anterior fontanelle. However, for a more detailed visualization of the 4th ventricle and the cerebral aqueduct, the temporal, mastoid or foramen magnum view should be preferably used (Figure 42). If ventricular enlargement is suspected, it should be confirmed and quantified with standardized measurements facilitating later review and objective evaluation of progression in serial scans (Figure 43) (19).

The most commonly used parameters to quantify the size of lateral ventricles include the ventricular index (Levene Index, VI) (Figure 43), the anterior horn width (AHW) (Figure 43), and the thalamo-occipital distance (Figure 43) (19, 20). The ventricular index and AHW are measured in the coronal plane at the level of the Foramina of Monro, while the thalamo-occipital distance is assessed in the parasagittal plane on each side (Figure 43).

Figure 42 Posthemorrhagic hydrocephalus in a preterm infant after intraventricular hemorrhage. CUS images in coronal (upper left), parasagittal (upper right), and axial (lower left) planes demonstrating posthemorrhagic hydrocephalus with dilatation of the entire ventricular system. The coronal plane (upper left) shows markedly enlarged lateral ventricles (1), third ventricle (2), and fourth ventricle (4). The parasagittal plane (upper right) demonstrates the dilated third ventricle (2) and cerebral aqueduct (3, arrow) in continuity with the enlarged fourth ventricle (4), confirming involvement of all ventricular compartments. The axial plane (lower left) provides a complementary view of the dilated lateral ventricles (1), third ventricle (2), aqueduct (3, arrow), and fourth ventricle (4), illustrating the global nature of the ventricular dilatation. The dilatation of all four ventricles and the aqueduct is characteristic of posthemorrhagic hydrocephalus resulting from impaired CSF resorption rather than obstructive disease.

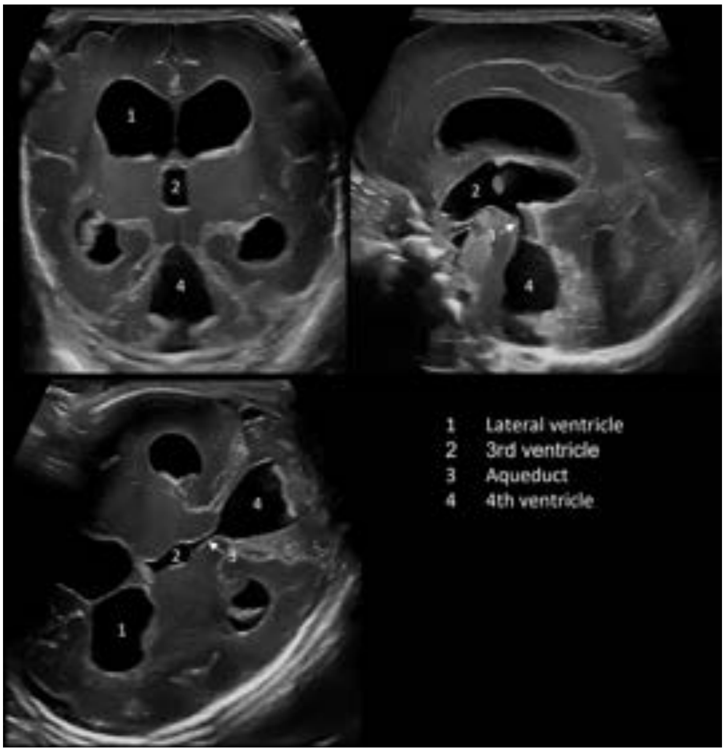

These measurements are useful not only for diagnosing hydrocephalus but also for guiding treatment (19, 21). In clinical practice, VI is plotted on gestational age–specific percentile curves, since the trajectory relative to the 97th percentile guides decision-making (20). Widely used reference curves cover 24 to 42 weeks (20) and have been extended to extremely preterm infants born at 23 to 27 weeks (22). Based on the EuroBrainUS Group consensus, neonatal ventriculomegaly is graded as mild (VI ≤ p97 and AHW ≤ 6 mm), moderate (VI between p97 and p97 + 4 mm, AHW 6–10 mm, or TOD > 25 mm), or severe (VI > p97 + 4 mm and/or AHW > 10 mm) (19). The latter represents the classical high thresholds for intervention in posthemorrhagic ventricular dilatation whereas the ELVIS-trail supports lower thresholds (21, 23). Beyond these quantitative measures, morphological features contribute to the differential diagnosis: "ballooning" of the frontal horns — rounded, outwardly convex walls reflecting raised intraventricular pressure — supports true hydrocephalus (Figure 42), whereas "angled", irregular ventricular horns are characteristic of ex-vacuo dilatation due to brain atrophy (Figure 33).

Ventricular dilation has three principal causes that require distinction: (1) obstructive (non-communicating) hydrocephalus (e.g., aqueduct stenosis, compressive tumor, congenital malformations); (2) ex-vacuo dilation due to brain volume loss (brain atrophy); and (3) communicating hydrocephalus from impaired CSF resorption (e.g., post-hemorrhagic, post-inflammatory) (19). In the vast majority of post-hemorrhagic and post-inflammatory hydrocephalus cases, communication between the ventricles and the subarachnoid space remains intact and ventricular dilatation progresses due to impaired CSF resorption caused by inflammation and glial scarring in the pericerebellar subarachnoid space. However, in some instances, blood clots may obstruct key CSF pathways, including the Foramina of Monro, the cerebral aqueduct, the Foramen of Magendie, or the Foramina of Luschka. In post-inflammatory hydrocephalus, ventricular debris and septations can contribute to obstruction, potentially complicating the clinical course. Therefore, a thorough evaluation of the entire CSF system is important. During the acute phase of intraventricular hemorrhage (IVH) and CSF infections, hyperechoic ventriculitis may be observed, resulting from an inflammatory reaction of the ependymal lining of the ventricles.

Figure 43 Measurements of lateral ventricles in posthemorrhagic ventricular dilatation. Two CUS images demonstrating the standardized measurements used to quantify ventricular size in a preterm infant with posthemorrhagic ventricular dilatation. Left image: coronal plane at the level of the foramina of Monro showing measurement of the ventricular index (VI), defined as the distance from the midline to the lateral wall of the lateral ventricle, and the anterior horn width (AHW), defined as the internal diameter of the anterior horn measured perpendicular to the long axis of the ventricle. Right image: parasagittal plane demonstrating measurement of the thalamo-occipital distance (TOD), defined as the distance from the posterior border of the thalamus to the occipital horn. Serial measurements of VI, AHW, and TOD are essential for objective monitoring of ventricular dilatation progression and for guiding treatment decisions.

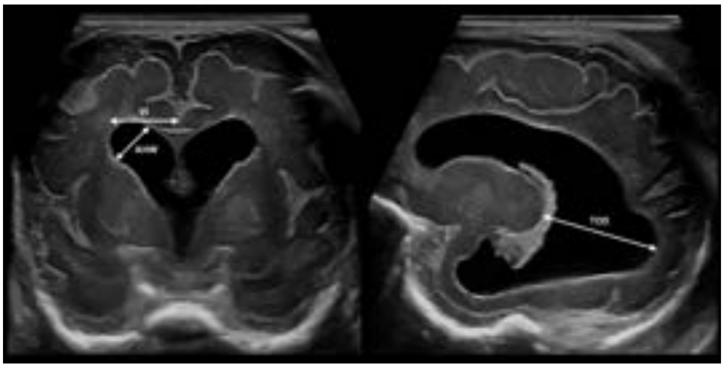

Germinal matrix, germinal matrix hemorrhage and intraventricular hemorrhage

The germinal matrix (GM) lining the entire ventricular system in the subependymal tissue of the ventricular walls gives rise to cerebral neuroblasts and glial cells that migrate centrifugally to the cortex (24). The thickness of the GM decreases by 24 weeks and almost completely involutes by 36-37 weeks, remaining longest in the area between head of caudate and thalamus (caudothalamic groove) (25). Due to its high proliferative activity, it is richly vascularized by thin and fragile vessels (25). Most, but not all, hemorrhages occur in the area of the caudothalamic groove in the first week of life (26). Germinal matrix hemorrhages (GMH) present as hyperechoic protrusions in the affected area (Figure 44).

Figure 44 Germinal matrix hemorrhage and intraventricular hemorrhage. CUS images in coronal (upper row) and parasagittal (lower row) planes demonstrating the spectrum of germinal matrix hemorrhage (GMH) and intraventricular hemorrhage (IVH). Upper row three coronal planes illustrating different locations of GMH, indicated by arrowheads — lateral to the caudate head at the caudothalamic groove (left), in the central subependymal region (middle), and more laterally with extension towards the ventricular system (right). Lower row: three parasagittal planes demonstrating the grading of GMH/IVH. Isolated GMH without ventricular involvement (Grade I, left image, arrowhead); IVH filling less than 50% of the ventricular lumen (Grade II, middle image); and IVH filling more than 50% of the ventricular lumen with ventricular dilatation (Grade III, right image). The parasagittal plane is the optimal view for grading GMH/IVH, as it allows clear visualization of the relationship between the intraventricular blood and the ventricular system.

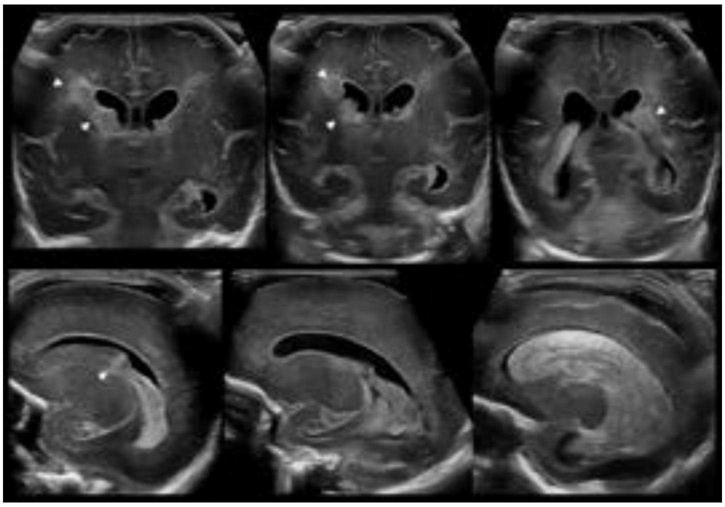

Hemorrhage entering the ventricular system is termed intraventricular hemorrhage (IVH) and is seen as echogenic clots within the ventricular system; color Doppler may demonstrate pulsatile CSF flow around the clots, later leading to hyperechogenic lining of the ventricular ependyma (ventriculitis) (26). GMH/IVH can occlude venous drainage pathways leading to periventricular hemorrhagic infarction (PHI) with fan-shaped appearance (Figure 37) (26). The location of the hemorrhagic infarction depends on the occluded vein, which influences the prognosis (27). GMH must be distinguished from cystic or hyperechogenic germinolysis sometimes called subventricular zone echogenicity which usually occurs later after the first week of life (Figure 45) (28, 29).

Figure 45 **Subventricular zone echogenicity in a preterm infant. CUS images in coronal (left and middle) and parasagittal (right) planes demonstrating subventricular zone echogenicity in a preterm infant. Symmetrical increased echogenicity is visible between the caudate head and the ventricular system, reflecting cystic or hyperechogenic germinolysis in the subependymal region. In contrast to germinal matrix hemorrhage, this finding occurs typically after the first week of life and shows a characteristic bilateral, symmetric distribution. The parasagittal plane (right image) demonstrates the typical location of the lesions along the subependymal layer, clearly distinguishable from intraventricular hemorrhage by the absence of echogenic material within the ventricular lumen.**

Midbrain, Brainstem and Cerebellum

Reliable evaluation of the midbrain, brainstem and cerebellum can only be achieved by using alternative acoustic windows like mastoid fontanelle, foramen magnum or the temporal acoustic window (4, 6, 7). However, not all pathologies can be visualized with high sensitivity due to the unfavorable location of these structures. The most important pathologies in this region are cerebellar hemorrhage (Figure 46) — often associated with germinal matrix hemorrhage and intraventricular hemorrhage — and cerebellar hypoplasia of prematurity (Figure 46, 47). Given their clinical relevance in preterm infants, sonographic examination of the cerebellum through the mastoid fontanelle should be part of every standard CUS protocol in this population.

Figure 46 **Cerebellar damage in preterm infants. CUS images obtained through the mastoid fontanelle demonstrating cerebellar hemorrhage and its sequelae in two preterm infants. Upper row: first patient with acute cerebellar hemorrhage — a median sagittal plane (upper left) shows a large hyperechogenic hemorrhage destroying the vermis, and a mastoid view (upper right) demonstrates the additional involvement of one cerebellar hemisphere and the mass effect on the surrounding posterior fossa structures. Lower row: second patient with the sequelae of a previous cerebellar hemorrhage — two axial planes (lower left and**

middle) and a mastoid view (lower right) demonstrate markedly reduced cerebellar volume with complete destruction of the normal cerebellar architecture, consistent with severe cerebellar hypoplasia resulting from post-hemorrhagic tissue destruction. A persistent Blake's pouch cyst in the posterior fossa can be seen in the midline. The comparison of the two patients illustrates the temporal evolution from acute hemorrhage to chronic cerebellar injury and hypoplasia.

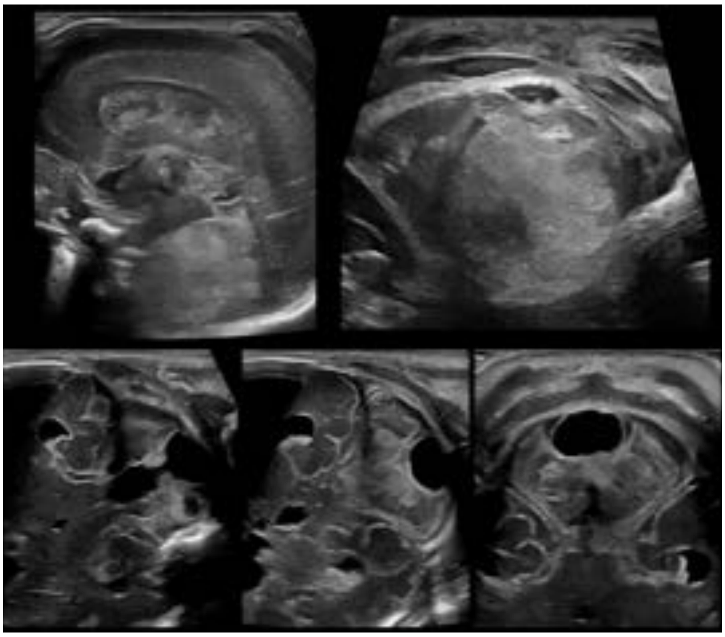

Figure 47 Cerebellar hypoplasia of prematurity after intraventricular hemorrhage and posthemorrhagic hydrocephalus. CUS images obtained through the anterior (left) and mastoid fontanelle (middle) in coronal and through the mastoid fontanelle in axial (right) planes demonstrating cerebellar hypoplasia of prematurity in the context of intraventricular hemorrhage. All planes show markedly dilated ventricular system with prominent temporal horns reflecting the hydrocephalus. The cerebellar hemispheres are reduced in volume and show an abnormal echogenicity pattern, consistent with cerebellar hypoplasia secondary to the combined effects of prematurity and posthemorrhagic injury. The right image additionally demonstrates the dilated temporal horns and the reduced posterior fossa volume in the axial plane.

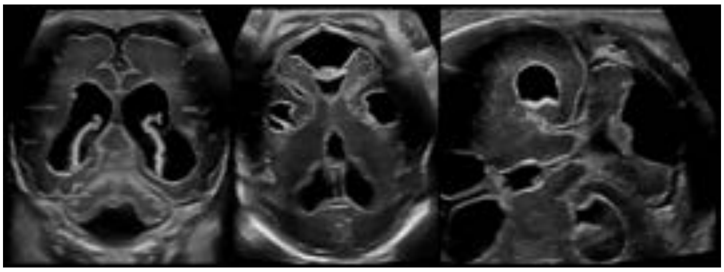

Central nervous system infections

Neonatal central nervous system (CNS) infections can cause a wide range of CUS changes, depending primarily on the pathogen. Recognizing the characteristic imaging features of each infection type is critical for timely diagnosis, treatment decisions, and outcome prediction (for a detailed review, see (13)).

The most common neonatal **bacterial CNS infections** are caused by *Group B Streptococcus (GBS)* and *Escherichia coli*. Typical findings are ventriculitis (increased echogenicity and thickening of the ventricular ependyma) (Figure 48), intraventricular strands, empyema, brain abscesses, and ischemic (stroke-like) lesions (13). Hydrocephalus may complicate the later course. More rarely, CNS infections with *Serratia, Citrobacter, Klebsiella, or Bacillus cereus* occur, which - beyond the abovementioned features - may cause colliquation necrosis capable of destroying extensive regions of cerebral tissue (Figure 49) (13).

Figure 48 Ventriculitis with increased echogenicity and thickening of the ventricular ependyma in bacterial CNS infection caused by Escherichia coli. CUS images in coronal (left) and parasagittal (right) planes demonstrating ventriculitis in a neonate with bacterial CNS infection. Both planes show markedly thickened and hyperechogenic ventricular ependyma lining the lateral ventricles, with loss of the normal thin, smooth appearance of the ventricular wall. Intraventricular strands and debris are visible within the ventricular lumen, reflecting the inflammatory exudate characteristic of bacterial ventriculitis. These findings indicate severe ependymal inflammation and are associated with a high risk of subsequent ventricular obstruction and hydrocephalus.

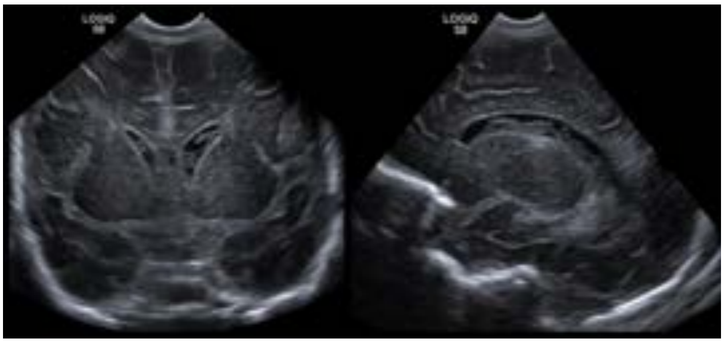

Figure 49 **Severe CNS infection with Serratia. CUS images in coronal and sagittal planes demonstrating the catastrophic progression of cerebral destruction in a neonate with Serratia CNS infection. Upper row (four days after first sepsis symptoms): coronal and sagittal planes show large areas of diffuse liquefying necrosis in both hemispheres with rapidly increasing parenchymal echogenicity, early cavitation, and progressive loss of normal brain architecture. Lower row (four weeks after first sepsis symptoms): coronal and sagittal planes demonstrate the resulting extensive brain destruction, with large debris-filled cavities, intraventricular strands, multiloculated abscesses, and CSF flow obstruction. The rapid and devastating progression from initial liquefying necrosis to complete structural destruction within four weeks is characteristic of Serratia and other Gram-negative bacterial CNS infections capable of producing colliquation necrosis.**

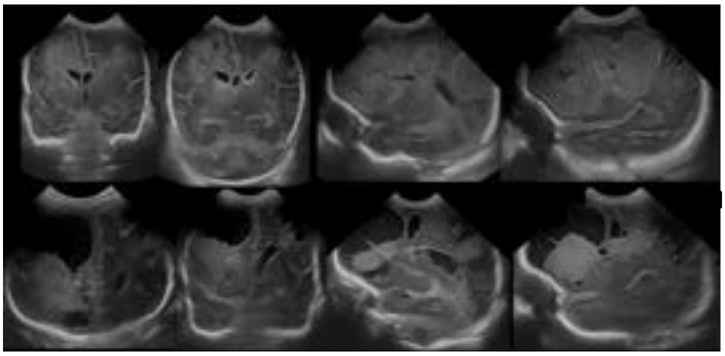

Perinatal viral CNS infections are far less common than bacterial CNS infections, with *herpes simplex virus (HSV)* and *enteroviruses* among the most frequent pathogens (13). The typical ultrasound finding is a marked hyperechogenicity of the periventricular white matter often followed by cystic degeneration. Typical CUS findings of **congenital cytomegalovirus (CMV) CNS infection** are germinolytic cysts, intraventricular septations, striatal vasculopathy, diffuse white matter hyperechogenicity, periventricular calcification, reduced brain volume, cerebellar hypoplasia, ventricular dilation, and cortical malformations (Figure 51). The most severe changes are found when CMV infection occurs in early fetal life.

Fungal CNS infections occur predominantly in very preterm infants and in newborns with immunodeficiency. Because early clinical symptoms may be deceptively mild, recognition of the characteristic imaging features is critical (13). *Candida albicans*, the most common pathogenic species, typically presents with a distinctive pattern of multiple round micro-abscesses that may involve the entire brain (Figure 50).

Parasitic CNS infections in neonates are dominated by congenital toxoplasmosis, with typical CUS findings of scattered intraparenchymal calcifications, ventriculomegaly or hydrocephalus, and — in severe early-gestational infection — parenchymal destruction with cortical and cerebellar volume loss. In contrast to CMV, cortical malformations are uncommon, and calcifications show no periventricular predilection (30). Other congenital parasitic infections (e.g. Chagas disease, malaria) rarely produce CNS findings detectable by CUS in the neonatal period (30).

Figure 50 Cerebral Candida infection. Two CUS images demonstrating the characteristic pattern of cerebral candidiasis in a very preterm infant. Both planes show multiple small, round hyperechogenic micro-abscesses distributed diffusely throughout the brain parenchyma, involving both hemispheres symmetrically and affecting the cortical and subcortical regions, and the deep grey matter structures. This distinctive pattern of disseminated micro-abscesses involving the entire brain is pathognomonic for cerebral Candida infection and requires urgent antifungal treatment.

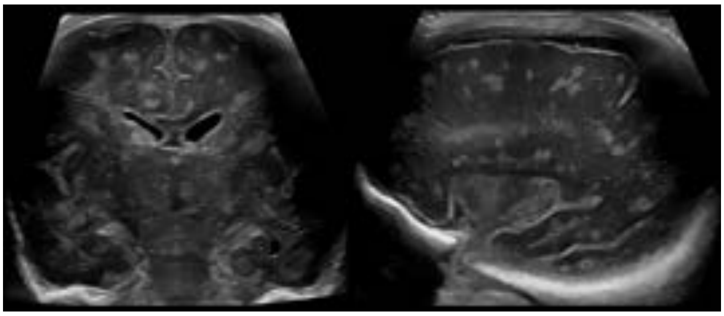

Figure 51 Congenital cytomegalovirus (CMV) CNS infection. CUS images in coronal and parasagittal planes demonstrating the characteristic spectrum of CUS findings in congenital CMV infection. Upper row: germinolytic cysts (asterisks) are visible in the parafrontal subependymal region (left and middle images) and in the caudothalamic groove (right image), representing a hallmark finding of congenital CMV. Lower row: striatal vasculopathy is indicated by dotted arrows (lower left and middle images), visible as echogenic linear structures along the lenticulostriate arteries; periventricular calcifications (arrowheads, lower middle and right images) appear as punctate hyperechogenic foci along the

ventricular walls. Together, these findings — germinolytic cysts, periventricular calcifications, and striatal vasculopathy — constitute the classical triad of congenital CMV CNS infection, with the most severe changes occurring when infection takes place in early fetal life.

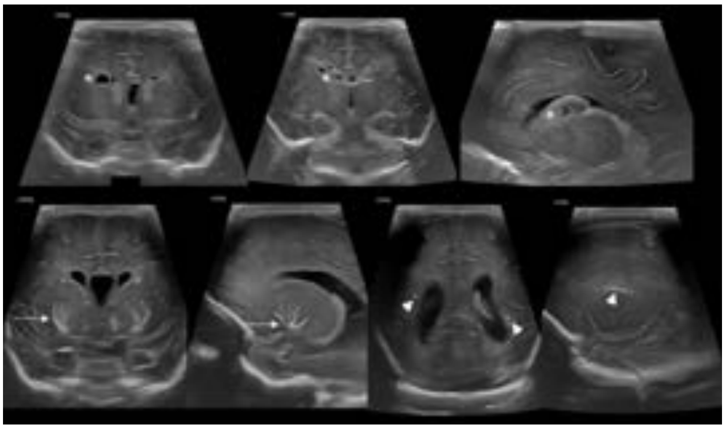

Conclusion

CUS is the primary imaging modality for assessing the neonatal brain at the bedside, offering a unique combination of safety, accessibility, and diagnostic power. To harness its full potential, optimal equipment settings, a thorough knowledge of normal neuroanatomy at different gestational ages, and familiarity with the most common neonatal brain pathologies are essential prerequisites. Systematic use of additional acoustic windows beyond the anterior fontanelle — including the posterior fontanelle, mastoid fontanelle, temporal acoustic window, and foramen magnum — significantly expands the range of detectable pathologies, particularly in regions that are difficult to assess through the anterior fontanelle alone, such as the parietal and occipital lobes, brainstem, cerebellum, and posterior fossa. Serial CUS examinations following standardized protocols are crucial for detecting the full spectrum of preterm and term brain injury and for monitoring its evolution over time. As imaging technology continues to advance, high-frequency linear probes in particular offer increasingly detailed visualization of superficial brain structures, further enhancing the diagnostic value of CUS in the most vulnerable patient population.

References

1. Dudink J, Jeanne Steggerda S, Horsch S, eur USbg. State-of-the-art neonatal cerebral ultrasound: technique and reporting. Pediatr Res. 2020;87(Suppl 1):3-12.
2. Annink KV, de Vries LS, Groenendaal F, Vijlbrief DC, Weeke LC, Roehr CC, et al. The development and validation of a cerebral ultrasound scoring system for infants with hypoxic-ischaemic encephalopathy. Pediatr Res. 2020;87(Suppl 1):59-66.

3. Agut T, Alarcon A, Cabanas F, Bartocci M, Martinez-Biarge M, Horsch S, et al. Preterm white matter injury: ultrasound diagnosis and classification. Pediatr Res. 2020;87(Suppl 1):37-49.
4. Fumagalli M, Parodi A, Ramenghi L, Limperopoulos C, Steggerda S, eur USbg. Ultrasound of acquired posterior fossa abnormalities in the newborn. Pediatr Res. 2020;87(Suppl 1):25-36.
5. D'Antoni AV, Donaldson OI, Schmidt C, Macchi V, De Caro R, Oskouian RJ, et al. A comprehensive review of the anterior fontanelle: embryology, anatomy, and clinical considerations. Childs Nerv Syst. 2017;33(6):909-14.
6. Correa F, Enriquez G, Rossello J, Lucaya J, Piqueras J, Aso C, et al. Posterior fontanelle sonography: an acoustic window into the neonatal brain. AJNR Am J Neuroradiol. 2004;25(7):1274-82.
7. Enriquez G, Correa F, Aso C, Carreno JC, Gonzalez R, Padilla NF, et al. Mastoid fontanelle approach for sonographic imaging of the neonatal brain. Pediatr Radiol. 2006;36(6):532-40.
8. de Vareilles H, Riviere D, Mangin JF, Dubois J. Development of cortical folds in the human brain: An attempt to review biological hypotheses, early neuroimaging investigations and functional correlates. Dev Cogn Neurosci. 2023;61:101249.
9. Nishikuni K, Ribas GC. Study of fetal and postnatal morphological development of the brain sulci. J Neurosurg Pediatr. 2013;11(1):1-11.
10. Stein A, Sody E, Bruns N, Felderhoff-Muser U. Development of an Ultrasound Scoring System to Describe Brain Maturation in Preterm Infants. AJNR Am J Neuroradiol. 2023;44(7):846-52.
11. Valverde E, Ybarra M, Bravo MC, Dudink J, Govaert P, Horsch S, et al. State-of-the-art cranial ultrasound in clinical scenarios for infants born at term and near-term. Dev Med Child Neurol. 2025;67(3):322-47.
12. Horsch S, Schwarz S, Arnaez J, Steggerda S, Arena R, Govaert P, et al. Cerebral Doppler imaging in neonates: A guide for clinical application and diagnosis. Dev Med Child Neurol. 2024;66(12):1570-89.
13. Licht-van der Stap RG, de Vries LS, Alarcon A, Govaert P, Steggerda SJ, Eur USBg. Cranial ultrasound in neonatal brain infections. Dev Med Child Neurol. 2025;67(8):986-1003.
14. de Goederen R, Raets MMA, Ecury-Goossen GM, de Jonge RCJ, Ramenghi LA, Koning IV, et al. Effect of Preterm Birth on Echogenicity in Basal Ganglia. Ultrasound Med Biol. 2017;43(10):2192-9.
15. Lu S, Brusic A, Gaillard F. Arachnoid Membranes: Crawling Back into Radiologic Consciousness. AJNR Am J Neuroradiol. 2022;43(2):167-75.
16. Skiold B, Hallberg B, Vollmer B, Aden U, Blennow M, Horsch S. A Novel Scoring System for Term-Equivalent-Age Cranial Ultrasound in Extremely Preterm Infants. Ultrasound Med Biol. 2019;45(3):786-94.
17. Libicher M, Troger J. US measurement of the subarachnoid space in infants: normal values. Radiology. 1992;184(3):749-51.
18. Fandak J, Markart S, Willems EP, Wildermuth S, Frauenfelder T, Fischer T, et al. Prospective measurement of the width of cerebrospinal fluid spaces by cranial ultrasound in neurologically healthy children aged 0-19 months. BMC Pediatr. 2024;24(1):315.
19. Bravo MC, Lubian S, Horsch S, Cabanas F, de Vries LS, Eur USBg. Neonatal ventriculomegaly: Pathophysiology and management guided with cranial ultrasonography. Dev Med Child Neurol. 2024;66(11):1419-31.
20. Brouwer MJ, de Vries LS, Groenendaal F, Koopman C, Pistorius LR, Mulder EJ, et al. New reference values for the neonatal cerebral ventricles. Radiology. 2012;262(1):224-33.
21. Cizmeci MN, Groenendaal F, Liem KD, van Haastert IC, Benavente-Fernandez I, van Straaten HLM, et al. Randomized Controlled Early versus Late Ventricular Intervention Study in Posthemorrhagic Ventricular Dilatation: Outcome at 2 Years. J Pediatr. 2020;226:28-35 e3.
22. Goeral K, Schwarz H, Hammerl M, Brugger J, Wagner M, Klebermass-Schrehof K, et al. Longitudinal Reference Values for Cerebral Ventricular Size in Preterm Infants Born at 23-27 Weeks of Gestation. J Pediatr. 2021;238:110-7 e2.

23. de Vries LS, Groenendaal F, Liem KD, Heep A, Brouwer AJ, van 't Verlaat E, et al. Treatment thresholds for intervention in posthaemorrhagic ventricular dilation: a randomised controlled trial. Arch Dis Child Fetal Neonatal Ed. 2019;104(1):F70-F5.
24. Maller VV, Cohen HL. Neonatal Head Ultrasound: A Review and Update-Part 1: Techniques and Evaluation of the Premature Neonate. Ultrasound Q. 2019;35(3):202-11.
25. Ballabh P. Pathogenesis and prevention of intraventricular hemorrhage. Clin Perinatol. 2014;41(1):47-67.
26. Parodi A, Govaert P, Horsch S, Bravo MC, Ramenghi LA, eur USbg. Cranial ultrasound findings in preterm germinal matrix haemorrhage, sequelae and outcome. Pediatr Res. 2020;87(Suppl 1):13-24.
27. Dudink J, Lequin M, Weisglas-Kuperus N, Conneman N, van Goudoever JB, Govaert P. Venous subtypes of preterm periventricular haemorrhagic infarction. Arch Dis Child Fetal Neonatal Ed. 2008;93(3):F201-6.
28. Epstein AA, Janos SN, Menozzi L, Pegram K, Jain V, Bisset LC, et al. Subventricular zone stem cell niche injury is associated with intestinal perforation in preterm infants and predicts future motor impairment. Cell Stem Cell. 2024;31(4):467-83 e6.
29. Horsch S, Kutz P, Roll C. Late germinal matrix hemorrhage-like lesions in very preterm infants. J Child Neurol. 2010;25(7):809-14.
30. Ni Leidhin C, Paddock M, Parizel PM, Warne RR, Shipman P, Lakshmanan R. Paediatric cranial ultrasound: abnormalities of the brain in term neonates and young infants. Insights Imaging. 2025;16(1):159.